Inorganic Chemistry

Article

pubs.acs.org/IC

Polyoxopalladates Encapsulating 8-Coordinated Metal Ions, $[MO_8Pd^{II}_{12}L_8]^{n-}$ (M = Sc^{3+}, Mn^{2+}, Fe^{3+}, Co^{2+}, Ni^{2+}, Cu^{2+}, Zn^{2+}, Lu^{3+}; L = $PhAsO_3^{2-}$, $PhPO_3^{2-}$, SeO_3^{2-})

Maria Barsukova-Stuckart,[†] Natalya V. Izarova,[†] Ryan A. Barrett,[‡] Zhenxing Wang,[‡] Johan van Tol,[‡] Harold W. Kroto,[‡] Naresh S. Dalal,*[,‡] Pablo Jiménez-Lozano,[§] Jorge J. Carbó,[§] Josep M. Poblet,[§] Marc S. von Gernler,[∥] Thomas Drewello,[∥] Pedro de Oliveira,[⊥] Bineta Keita,[⊥] and Ulrich Kortz*[,†]

[†]School of Engineering and Science, Jacobs University, P.O. Box 750 561, 28725 Bremen, Germany

[‡]Department of Chemistry and Biochemistry, Florida State University, 32306 Tallahassee, Florida, United States

[§]Department de Química Física i Inorgànica, Universitat Rovira i Virgili, 43007 Tarragona, Spain

[∥]Department of Chemistry and Pharmacy, University of Erlangen-Nürnberg, 91058 Erlangen, Germany

[⊥]Laboratoire de Chimie Physique, UMR 8000, CNRS, Equipe d'Electrochimie et de Photoélectrochimie, Université Paris-Sud, Bâtiment 350, 91405 Orsay Cedex, France

Supporting Information

ABSTRACT: A total of 16 discrete polyoxopalladates(II) $[MO_8Pd^{II}_{12}L_8]^{n-}$, with a metal ion **M** encapsulated in a cuboid-shaped $\{Pd_{12}O_8L_8\}$ cage, have been synthesized: the phenylarsonate-capped series (1) **L** = $PhAsO_3^{2-}$, **M** = Sc^{3+} (**ScPhAs**), Mn^{2+} (**MnPhAs**), Fe^{3+} (**FePhAs**), Co^{2+} (**CoPhAs**), Ni^{2+} (**NiPhAs**), Cu^{2+} (**CuPhAs**), Zn^{2+} (**ZnPhAs**); the phenylphosphonate-capped series: (2) **L** = $PhPO_3^{2-}$, **M** = Cu^{2+} (**CuPhP**), Zn^{2+} (**ZnPhP**); and the selenite-capped series (3) **L** = SeO_3^{2-}, **M** = Mn^{2+} (**MnSe**), Fe^{3+} (**FeSe**), Co^{2+} (**CoSe**), Ni^{2+} (**NiSe**), Cu^{2+}, (**CuSe**), Zn^{2+} (**ZnSe**), Lu^{3+} (**LuSe**)). The polyanions were prepared in one-pot reactions in aqueous solution of $[Pd_3(CH_3COO)_6]$ with an appropriate salt of the metal ion **M**, as well as $PhAsO_3H_2$, $PhPO_3H_2$, and SeO_2, respectively, and then isolated as hydrated sodium salts $Na_n[MO_8Pd^{II}_{12}L_8]\cdot yH_2O$ (y = 10−37). The compounds were characterized in the solid state by IR spectroscopy, single-crystal XRD, elemental and thermogravimetric analyses. The solution stability of the diamagnetic polyanions **ScPhAs**, **ZnPhAs**, **ZnPhP**, **ZnSe**, and **LuSe** was confirmed by multinuclear (^{77}Se, ^{31}P, ^{13}C, and ^{1}H) NMR spectroscopy. The polyoxopalladates **ScPhAs**, **MnPhAs**, **CoPhAs**, and **CuPhAs** were investigated by electrospray ionization mass spectrometry (ESI-MS) and tandem mass spectrometry (MS/MS). Electrochemical studies on the manganese- and iron-containing derivatives demonstrated that the redox properties of the Mn^{2+}, Fe^{3+}, and Pd^{2+} centers in the polyanions are strikingly influenced by the nature of the capping group. These results have subsequently been verified by density functional theory (DFT) calculations. Interestingly, electron paramagnetic resonance (EPR) measurements suggest that the coordination geometry around Mn^{2+} is dynamically distorted on the EPR time scale ($\sim 10^{-11}$ s), whereas it appears as a static ensemble with cubic symmetry on the X-ray diffraction (XRD) time-scale (10^{-15} s). The octacoordinated Cu^{2+} cuboid is similarly distorted, in good agreement with DFT calculations. Interestingly, $g_{\|}$ is smaller than $g_{\perp}$, which is quite unusual, needing further theoretical development.

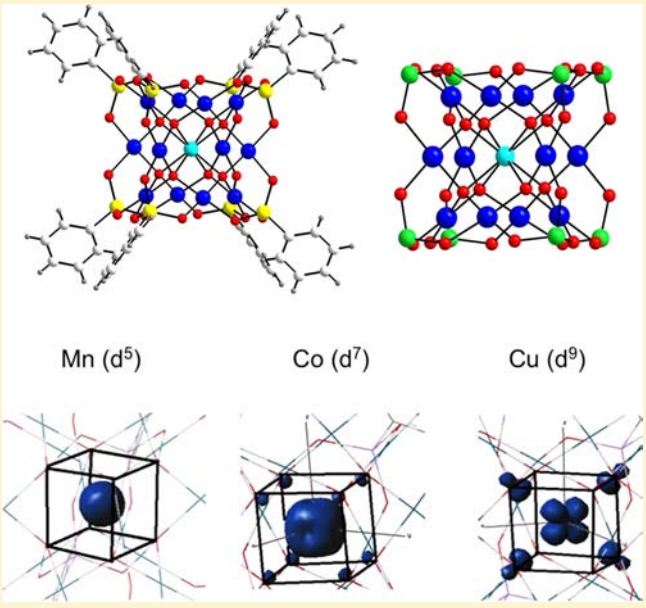

INTRODUCTION

Polyoxometalates (POMs) comprise a large class of nanosized, polynuclear metal-oxo anions that exhibit a wide compositional and structural diversity as well as a broad range of physical and chemical properties making them attractive for applications in different areas such as catalysis, medicine, magnetism, bio- and nanotechnology.[1] POMs are usually formed by group V and VI metal ions in high oxidation states (e.g., V^{5+}, Nb^{5+}, Mo^{6+}, Ta^{5+}, and W^{6+}),[1] but several polyanions comprising U^{6+},[2a] Sb^{5+},[2b] and

Received: July 17, 2012
Published: November 29, 2012

   dx.doi.org/10.1021/ic301537n | *Inorg. Chem.* 2012, 51, 13214−13228

$Mn^{2+/3+}$,[2c] as well as late transition metals, Pd^{2+}, Pt^{3+} and Au^{3+},[3−5] are known. POMs of the latter subclass, based on noble metal addenda, are expected to be important as precursors for nanoparticle synthesis and could be used as promising models to understand the mechanism in noble metal based catalysis.[6]

In 2008 Kortz's group discovered a simple one-pot procedure for the synthesis of late transition metal-oxo complexes in aqueous media by condensation of $[Pd(H_2O)_4]^{2+}$ ions in the presence of capping groups such as simple oxoanions, leading to the first polyoxopalladate(II), $[Pd^{II}_{13}As^{V}_{8}O_{34}(OH)_6]^{8-}$ (**$Pd_{13}As_8$**), which can be described as a $\{Pd_{12}O_8(AsO_4)_8\}$ nanocube encapsulating a central Pd^{2+} ion with square-planar coordination.[3a] Attempts to rationally prepare other members of this novel and unexpected class of compounds have resulted in the isolation of several novel polypalladates(II), namely, the cube-shaped $[Pd^{II}_{13}O_8(PhAsO_3)_8]^{6-}$ (**$Pd_{13}(PhAs)_8$**) and $[Pd^{II}_{13}O_8(SeO_3)_8]^{6-}$ (**$Pd_{13}Se_8$**),[3b] the pentagonal star-shaped $[Pd^{II}_{15}O_{10}(SeO_3)_{10}]^{10-}$,[3c] $[Pd^{II}_{15}O_{10}(PO_4)_{10}]^{20-}$, $[Pd^{II}\subset Pd^{II}_{15}O_{10}(PO_4)_{10}]^{18-}$,[3d] and $[Pd^{II}_{2}\subset H_7Pd^{II}_{15}O_{10}(P^{V}O_4)_{10}]^{13-}$,[3e] the mixed-metal, bowl-shaped $[Pd^{II}_{7}V^{V}_{6}O_{24}(OH)_2]^{6-}$,[3f] as well as the double-cuboid-shaped 22-palladate(II) $[Cu_2Pd^{II}_{22}P_{12}O_{60}(OH)_8]^{20-}$ (**$Pd_{22}Cu_2P_{12}$**).[3g] We have also shown that the central palladium(II) ion in **$Pd_{13}(PhAs)_8$** can be replaced by lanthanide and yttrium ions, resulting in the large (13 members) family **$LnPd_{12}(PhAs)_8$**.[3h] Very recently, we also reported on a series of 3d metal-centered, cube-shaped, phosphate-capped polyoxopalladates(II) **$MPd_{12}P_8$** (**M** = Mn^{2+}, Fe^{3+}, Co^{2+}, Cu^{2+}, Zn^{2+}), where the heterometal ion **M** plays the role of a central guest in the cuboid $\{Pd^{II}_{12}O_8(PO_4)_8\}$ shell and possesses a highly unusual cubic coordination geometry.[3i] Interestingly, these phosphate-capped polypalladates could not be obtained in the absence of 3d metal ions (e.g., the hypothetical "**$Pd_{13}P_8$**" and "**$LnPd_{12}P_8$**" are still unknown), which reveals an important structure-directing role of the central metal ion in the **M**/Pd^{2+}/PO_4 system. Very recently, the large $[Pd_{84}O_{42}(OAc)_{28}(PO_4)_{42}]^{70-}$ wheel has been reported.[3j]

Our continued investigation on this system, and in particular the possibility to incorporate metal ions **M** in the cavity of the $\{Pd_{12}O_8L_8\}$ shell, has led to a novel series of polypalladates with the general formula $[MO_8Pd^{II}_{12}L_8]^{n-}$, where (1) **L** = $PhAsO_3^{2-}$, **M** = Sc^{3+} (**ScPhAs**), Mn^{2+} (**MnPhAs**), Fe^{3+} (**FePhAs**), Co^{2+} (**CoPhAs**), Ni^{2+} (**NiPhAs**), Cu^{2+} (**CuPhAs**), Zn^{2+} (**ZnPhAs**); (2) **L** = $PhPO_3^{2-}$, **M** = Cu^{2+} (**CuPhP**), Zn^{2+} (**ZnPhP**), which are the first examples of polyoxopalladates with $PhPO_3^{2-}$ as capping group; and (3) **L** = SeO_3^{2-}, **M** = Mn^{2+} (**MnSe**), Fe^{3+} (**FeSe**), Co^{2+} (**CoSe**), Ni^{2+} (**NiSe**), Cu^{2+} (**CuSe**), Zn^{2+} (**ZnSe**), Lu^{3+} (**LuSe**). Here, we report on the synthesis, structure, NMR and mass spectrometry studies as well as electrochemistry, density functional theory (DFT) calculations, and magnetic properties of three heteropolyoxopalladate(II) families. The central metal ion exhibits unusually perfect cubic coordination in the polyanions with $PhAsO_3^{2-}$ and $PhPO_3^{2-}$ capping groups, and distorted cubic geometry in the polyoxopalladatoselenites, as shown by single-crystal X-ray analysis. Such a high coordination number is rather unusual for 3d transition metal ions, and only a few examples are known.[2c,3g,i,k,7]

During the preparation of our manuscript a publication reporting the selenite-capped derivatives $[MO_8Pd^{2+}_{12}(SeO_3)_8]^{6-}$ (**M** = Mn^{2+}, Co^{2+}, Ni^{2+}, Cu^{2+}, Zn^{2+}) by Hu and coworkers appeared in the literature.[3k] However, our synthetic procedures for **MSe** are different from those of Hu, and so is the unit cell for **CuSe**.[3k] Also, in contrast to Hu's group, we studied the solution stability of the diamagnetic derivatives **ZnSe** and **LuSe** by ^{77}Se NMR and we also performed electrochemical studies on **MnSe**, **FeSe**, and **NiSe**. Moreover, we report for the first time the iron(III)- and lutetium(III)-containing, selenite-capped dodecapalladates(II) $[Fe^{III}O_8Pd^{II}_{12}(SeO_3)_8]^{5-}$ (**FeSe**) and $[Lu^{III}O_8Pd^{II}_{12}(SeO_3)_8]^{5-}$ (**LuSe**).

RESULTS AND DISCUSSION

Synthesis and Structure. Polyanions $[MO_8Pd^{II}_{12}L_8]^{n-}$ were prepared in simple one-pot reactions of $[Pd_3(CH_3COO)_6]$, phenylarsonic acid or phenylphosphonic acid or selenium dioxide, and an appropriate salt of the metal ion **M** in aqueous sodium acetate solution. It should be noted that the synthesis of the phenylphosphonate-capped palladates required adjustment of the pH to 8.0, which is unusual in polyoxopalladate synthesis, and for the derivatives **CuPhP** and **ZnPhP** different concentrations of the acetate buffer are needed, namely, 0.5 and 2.0 M, respectively. The polyanions were isolated as hydrated sodium salts $Na_n[MO_8Pd^{II}_{12}L_8]\cdot yH_2O$ (**Na-ML**) with yields ranging from 16% (for **Na-ScPhAs**) to 79% (for **Na-ZnSe**). These compounds are stable toward air and light in the solid state and can be successfully recrystallized several times from aqueous sodium acetate solution at the same pH value used for the original synthesis.

All our efforts to incorporate palladium(II) or lanthanide(III) ions in the center of the cuboid 12-palladate shell $\{Pd^{II}_{12}O_8(PhPO_3)_8\}$ were unsuccessful, fully consistent with the polyoxopalladatophosphates **$MPd_{12}P_8$**,[3i] but in contrast to the phenylarsonate-capped **$Pd_{13}(PhAs)_8$** and **$LnPd_{12}(PhAs)_8$**.[3b,h] This fact further supports our hypothesis that the type of capping group influences the dimension of the central cavity of the 12-palladate shell $\{Pd^{II}_{12}O_8L_8\}$ and hence its ability to incorporate metal ions of different size.[3h,i]

For the synthesis of **MSe** we used about four times higher concentrations of reagents (0.125 M vs 0.03 M Pd^{2+} and Se^{4+} by Hu et al.) and a **M**: Pd: Se ratio of 1: 12: 12 vs 2: 12: 12 by Hu et al.[3k] Our reactions were also performed at higher pH (6–7 vs 5), as well as higher temperature and shorter times of heating. This allowed for significantly higher yields for the **CoSe**, **CuSe**, and **ZnSe** in our case, whereas the yield was the same for the Ni^{2+} centered analogue **NiSe**, and twice lower for the Mn^{2+}-containing polyanion **MnSe**. This also reflects the importance of pH, reagent ratios and concentrations, and reaction temperatures during the formation of the structural family **$MPd_{12}Se_8$**.

Single-crystal X-ray analysis revealed that the compounds of the first two series **Na-MPhAs** and **Na-MPhP** are isomorphous, all crystallizing in the tetragonal crystal system with space group $I4/m$. Polyanions **MPhP** are the first examples of polyoxopalladates(II) with organophosphonate capping groups. The structure of $\{MPd_{12}O_8(PhX^{V}O_3)_8\}$ (X = As, P) in **MPhAs** and **MPhP** is very similar to the previously reported **$Pd_{13}(PhAs)_8$**.[3b] The main difference is that the central octacoordinated Pd^{2+} ion in the latter has now been replaced by a 3d transition metal ion (see Figure 1a), which is coordinated by eight oxygen atoms, forming a regular cube. The 12 palladium(II) ions surrounding the central $\{MO_8\}$ fragment in **MPhAs** and **MPhP** form a cuboctahedron. Each oxygen atom of the "inner" $\{MO_8\}$ cube (μ_4-O) is coordinated by the central guest ion M^{n+} and three palladiums, situated on a trigonal face of the cuboctahedron. Each of the 12 Pd^{2+} ions

dx.doi.org/10.1021/ic301537n | Inorg. Chem. 2012, 51, 13214–13228

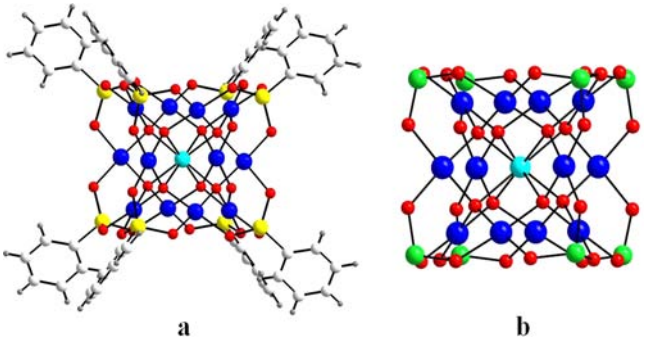

Figure 1. Ball-and-stick representation of: $[MO_8Pd^{II}_{12}(X^VPhO_3)_8]^{n-}$ (a) and $[MO_8Pd^{II}_{12}(SeO_3)_8]^{n-}$ (b). Color code: M, turquoise; Pd, blue; O, red; Se, green; X = As, P, yellow; C, white; H, gray.

exhibits the expected square-planar coordination by 2 μ_4-O and 2 "outer" oxygen atoms (μ_2-O). The 24 "outer" oxygen atoms form a truncated cube-shaped shell, which is capped either by 8 $AsPh^{4+}$ (**MPhAs**) or by PPh^{4+} (**MPhP**) groups, where As^{5+} and P^{5+} ions possess tetrahedral coordination geometry. The 8 arsenic(V) or phosphorus(V) ions in fact form an external, distorted cube-shaped shell. Selected bond distances for polyanions **MPhAs** and **MPhP** are shown in Table 1.

In the solid state the polyanions **MPhAs** and **MPhP** form the same hexagonal-packing framework with channels along the *a* and *b* axes as $\mathbf{Pd_{13}(PhAs)_8}$[3b] and $\mathbf{LnPd_{12}(PhAs)_8}$[3h] (see Supporting Information (SI), Figure S1). The channels are occupied by sodium cations and crystal water molecules. Neighboring polyanions are connected through weak CH-π hydrogen bonds,[8] which are directed along diagonals between the *b* and *c*, and the $-b$ and $-c$ axes. There are no $\pi-\pi$ stacking interactions between the phenyl groups, which could be explained by mutual repulsion of the hydrophobic aromatic groups and also the hydrophilic polyoxopalladate cores, as well as the positioning of the organic groups relative to each other.

The structure of the polyoxopalladates $[MO_8Pd^{II}_{12}(SeO_3)_8]^{n-}$ (**MSe**) of the third series reported here resembles the parent ion $[Pd^{II}_{13}O_8(SeO_3)_8]^{6-}$,[3b] but now a 3d transition metal ion occupies the central position instead of the six-coordinated Pd^{2+} ion, and the former is bound by eight oxygen atoms situated at the vertices of a distorted cube (see Figure 1b). In general, the structure of polyanions **MSe** can be described in analogy to the $\{MPd_{12}O_8(PhXO_3)_8\}$ core in **MPhAs** and **MPhP** (see above), but in **MSe** the truncated cube-shaped shell is capped by eight Se^{4+} ions, which exhibit a trigonal-pyramidal geometry with an external, stereochemically active lone pair. Selected bond distances for polyanions **MSe** are shown in Table 2.

The hydrated sodium salts of polyanions **MSe** (M = Mn^{2+}, Fe^{3+}, Co^{2+}, Ni^{2+}, and Zn^{2+}) are isomorphous and crystallize in orthorhombic symmetry in the *Pnma* space group. The polyanions in such crystals are linked by sodium ions and form zigzag layers perpendicular to the crystallographic *a* axis (Figure 2a). The Cu^{2+}-centered derivative **Na-CuSe** crystallizes in monoclinic symmetry, forming pseudochains along the *c* axis (Figure 2b). Within every chain a lone pair of one of the seleniums per polyanion is directed toward the center of the neighboring polyanion (Figure 2c). Short Se···Se contacts (4.22–4.33 Å) and Na^+ counter cations link the chains in the 3D framework.

In the solid state polyanions **LuSe** form a porous square grid framework, where the voids are occupied by sodium cations and crystal water molecules (Figure 2d).

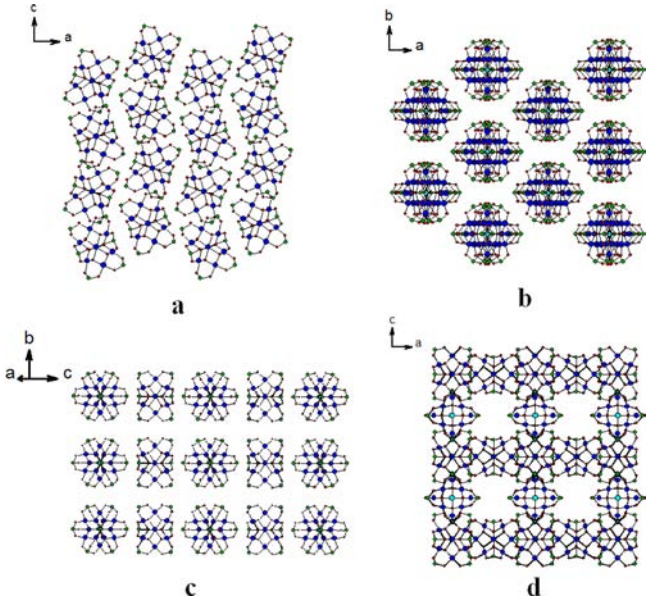

Figure 2. Crystal packing arrangement of polyanions in **Na-MSe** (M = Mn^{2+}, Fe^{3+}, Co^{2+}, Ni^{2+}, and Zn^{2+}) along the *b* axis (a); along the *c* axis (b), and a view of the pseudochains in **Na-CuSe** (c); and in **Na-LuSe** (d). Sodium counter cations and crystal waters omitted for clarity. The color code is the same as in Figure 1.

NMR Studies. We investigated the solution stability of the diamagnetic polyanions **ScPhAs**, **ZnPhAs**, **ZnPhP**, **ZnSe**, and **LuSe** by multinuclear NMR spectroscopy. Polyanions **ScPhAs**, **ZnPhAs**, and **ZnPhP** were studied in H_2O/D_2O solution by ^{13}C and ^1H NMR. The spectra show the expected patterns for phenyl groups (see Figures S2–S7). In addition, the phenyl-

Table 1. Selected Bond Distances/Å for Polyanions MPhAs and MPhP

	M–(μ_4-O)	Pd–(μ_4-O)	Pd–(μ_2-O)	X–(μ_2-O)	X–C
ScPhAs	2.257(4)	1.978(4)–1.981(4)	2.027(5)–2.037(5)	1.681(5)–1.693(5)	1.908(6)
MnPhAs	2.294(5)	1.966(5)–1.979(5)	2.038(6)–2.045(6)	1.663(7)–1.674(7)	1.914(8)
FePhAs	2.224(5)	1.965(5)–1.978(5)	2.042(5)–2.049(5)	1.669(6)–1.683(6)	1.895(8)
CoPhAs	2.259(6)	1.953(6)–1.988(6)	2.030(7)–2.045(7)	1.676(7)–1.688(7)	1.910(9)
NiPhAs	2.276(7)–2.277(7)	1.950(6)–1.981(6)	2.030(7)–2.051(7)	1.667(7)–1.675(7)	1.917(10)
CuPhAs	2.270(4)	1.967(3)–1.971(3)	2.037(4)–2.052(4)	1.685(4)–1.688(3)	1.903(4)
ZnPhAs	2.269(7)	1.962(7)–1.977(7)	2.039(8)–2.050(7)	1.673(8) –1.687(8)	1.892(11)
CuPhP	2.242(8)	1.953(7)–1.964(7)	2.045(8)–2.068(8)	1.530(9)–1.536(9)	1.801(13)
ZnPhP	2.239(5)	1.953(4)–1.963(5)	2.061(5)–2.064(5)	1.534(6)–1.539(5)	1.793(7)

dx.doi.org/10.1021/ic301537n | *Inorg. Chem.* 2012, 51, 13214–13228

Table 2. Selected Bond Distances/Å for Polyanions MSe

	M−(μ_4-O)	Pd−(μ_4-O)	Pd−(μ_2-O)	Se−(μ_2-O)
MnSe	2.219(14)−2.261(14)	1.936(14)−2.010(20)	2.017(16)−2.090(30)	1.670(20)−1.746(13)
FeSe	2.149(16)−2.236(17)	1.890(16)−1.983(9)	2.021(12)−2.061(18)	1.659(19)−1.724(13)
CoSe	2.190(20)−2.260(20)	1.927(16)−1.980(16)	2.012(17)−2.080(30)	1.665(19)−1.740(17)
NiSe	2.120(12)−2.317(14)	1.941(9)−1.975(7)	2.033(10)−2.08(2)	1.685(13)−1.722(10)
CuSe	2.113(14)−2.319(12)	1.912(12)−1.989(7)	2.017(10)−2.079(15)	1.663(11)−1.714(10)
ZnSe	2.180(20)−2.250(20)	1.941(19)−1.990(20)	2.033(17)−2.077(18)	1.665(18)−1.720(30)
LuSe	2.269(19)−2.324(17)	1.958(10)−1.975(19)	2.01(2)−2.04(2)	1.681(17)−1.705(13)

phosphonate-capped Zn^{2+} derivative **ZnPhP** was investigated by ^{31}P NMR spectroscopy, see Figure 3. The observed singlet

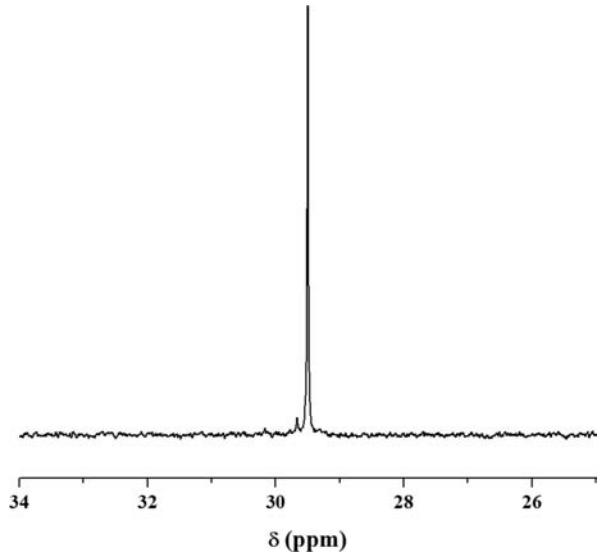

Figure 3. ^{31}P NMR spectrum of **Na-ZnPhP** at room temperature in H_2O/D_2O.

at 29.5 ppm (compared to free phenylphosphonate which resonates at 12.0 ppm in aqueous solution at similar pH) clearly shows that the polyanion remains intact. This is fully consistent with the presence of eight magnetically equivalent P nuclei in **ZnPhP**, as seen by single crystal XRD. This result unambiguously proves the solution stability of the polyanion.

Similarly, the ^{77}Se NMR spectra of **ZnSe** and **LuSe** derivatives in H_2O/D_2O at around pH 6.4 (Figure 4) revealed the expected singlet (at 1222.5 ppm for **ZnSe** and 1223.8 ppm for **LuSe**), fully consistent with the crystal structure and thus indicating solution stability of the polyanions. For comparison, selenium dioxide dissolved in water at pH 6.4 showed a singlet in ^{77}Se NMR at 1316.3 ppm.

Earlier we also observed a singlet in the ^{31}P NMR spectrum of $\mathbf{ZnPd_{12}P_8}$ in aqueous solution.[3i] Thus, our multinuclear NMR studies unambiguously prove the stability of the $\mathbf{MPd_{12}L_8}$ structural type in aqueous solution, which is a good basis for further applications of these polyanions in solution, for example, in homogeneous catalysis or as precursors for monodisperse nanoparticles.

IR spectra. The FT-IR spectra of the polyoxopalladates in **Na-MPhAs** are similar to those of the parent species $\mathbf{Pd_{13}(PhAs)_8}$[3b] and $\mathbf{LnPd_{12}(PhAs)_8}$.[3h] The same applies to **MSe** and their parent ion $\mathbf{Pd_{13}Se_8}$.[3b] For **Na-CuPhP** and **Na-ZnPhP** the FT-IR spectra are virtually identical with only slight shifts of some band positions relative to each other. As representative examples the FT-IR spectra of **Na-ScPhAs**, **Na-CuPhP**, and **Na-MnSe** are shown in Figures S8−S10.

For all compounds the bands between 400 and 660 cm^{-1} can correspond to Pd−O as well as M−O vibrations, and the broad band around 1630 cm^{-1} is associated with asymmetric vibrations of the crystal waters. The FT-IR spectra of **Na-MPhAs** showed a strong band at ∼805 cm^{-1} corresponding to vibrations of the {AsO_3} heterogroup fragments, as well as

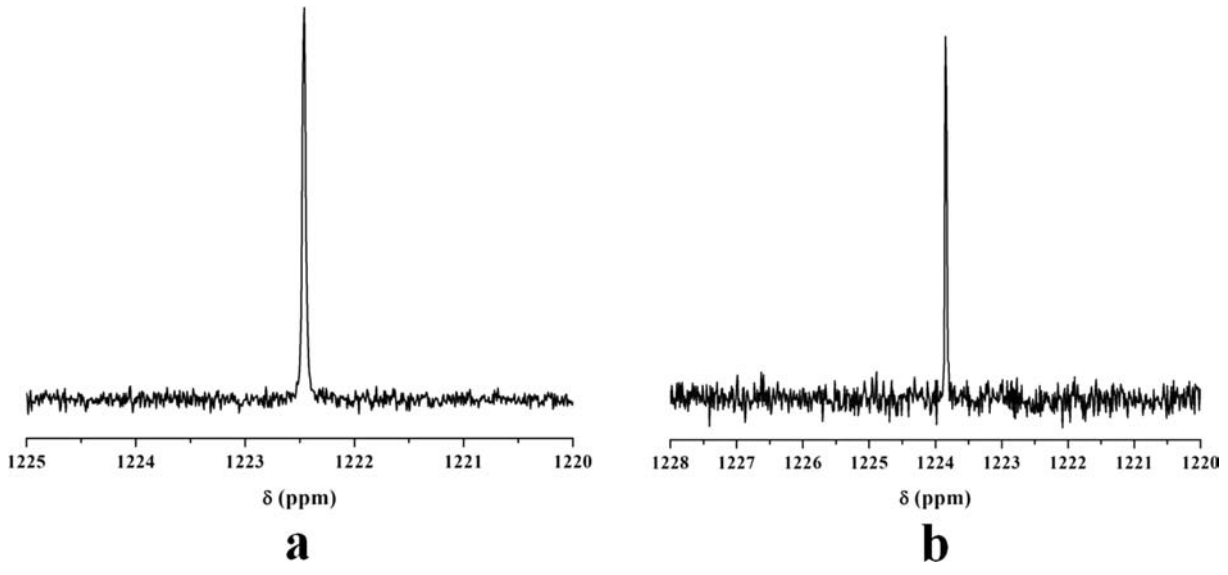

Figure 4. ^{77}Se NMR spectra of **Na-ZnSe** (a) and **Na-LuSe** (b) at room temperature in H_2O/D_2O.

dx.doi.org/10.1021/ic301537n | *Inorg. Chem.* 2012, 51, 13214−13228

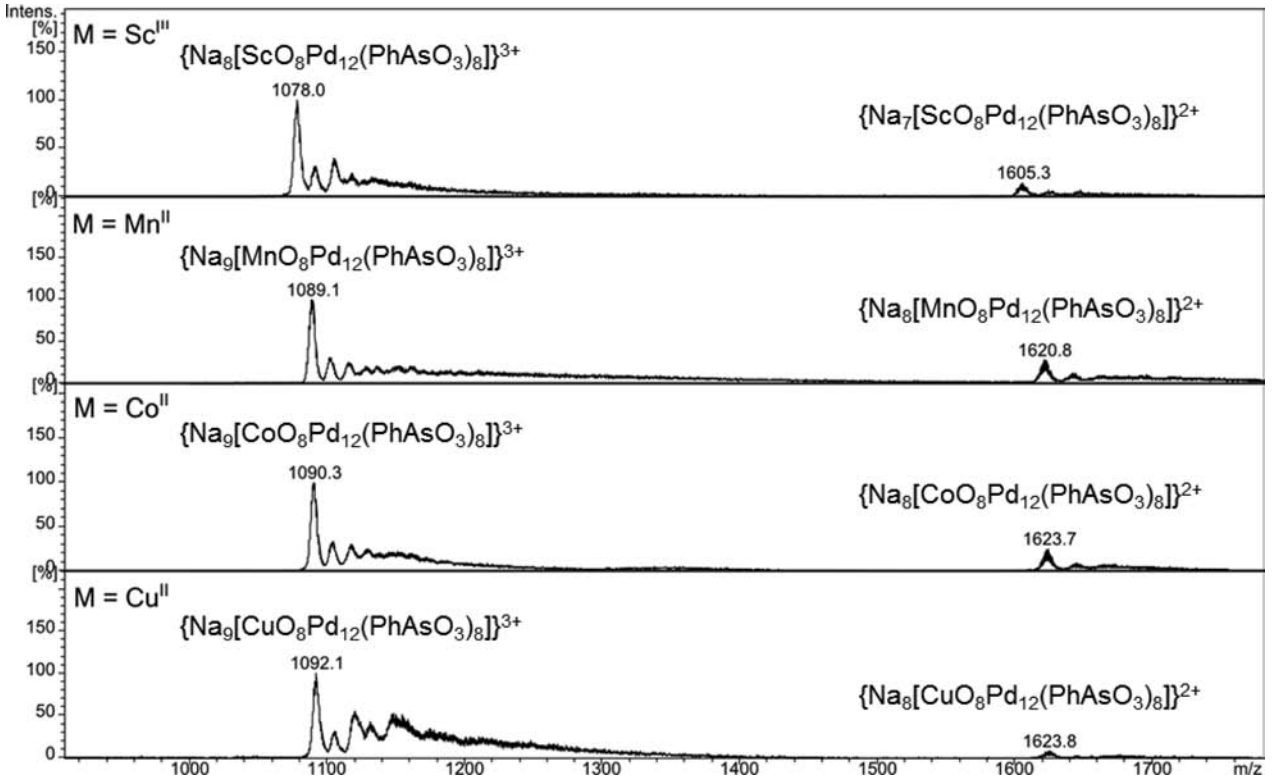

Figure 5. Positive ion ESI mass spectra of **ScPhAs**, **MnPhAs**, **CoPhAs**, and **CuPhAs**.

bands at 695, 742 and between 1090 and 1480 cm^{-1}, which belong to bending and stretching vibrations of the C−H and C−C bonds of the phenyl rings. For **Na-CuPhP** and **Na-ZnPhP** the strong bands at 940, 1039, and 1130 cm^{-1} are attributed to P−O vibrations, and the vibrations of the phenyl groups appear in the region 700−760 cm^{-1} and at 1436 and 1482 cm^{-1}, respectively. In the case of **Na-MSe** the vibrations of the SeO_3^{2-} heterogroups appear around 735 and 795 cm^{-1}, respectively.[9]

Thermogravimetric Analysis (TGA). The thermal stability of the hydrated salts of **MPhAs**, **MPhP**, and **MSe** was investigated on crystalline samples by thermogravimetric analysis under nitrogen atmosphere.

In line with the structural similarity of the polyoxopalladates, we observed very similar thermograms for both series **Na-MPhAs**, **Na-CuPhP** and **Na-ZnPhP**. For **Na-ScPhAs** (Figure S11) the first weight loss step occurs between 25 and 220 °C and corresponds to the removal of 19 water molecules per formula unit (9.7% found vs 9.8% calc), whereas for **Na-CuPhP** (Figure S12) it occurs between 25 and 200 °C and corresponds to the loss of 29 crystal waters (15.4% found vs 15.5% calc). The combustion of eight phenyl groups per formula unit proceeds in the temperature range 220−460 °C (17.3% found vs 17.6% calc) for **Na-ScPhAs** and between 200 and 550 °C (18.4% found vs 18.3% calc) for **Na-CuPhP**.

The thermogravimetric processes of the polyoxopalladates of the third series **Na-MSe** are also very similar and reveal several weight-loss steps. For **Na-MnSe** (Figure S13) the first weight loss step in the TGA curve is between 25−200 °C and corresponds to the loss of the 10 crystal waters per formula unit (6.1% found vs 6.5% calc). Several consecutive weight loss steps occur in the temperature range 200−820 °C and are attributed to the release of 8 SeO_2 molecules per formula unit (30.7% found vs 31.8% calc). The total observed weight loss for **Na-MnSe** at 1000 °C is 44%.

Mass Spectrometry. The ESI mass spectra of **ScPhAs**, **MnPhAs**, **CoPhAs**, and **CuPhAs** are depicted in Figure 5. The overall appearance of the mass spectra is strikingly similar. Within the experimentally accessible mass range (m/z 50−6000), there are in all cases only two regions featuring distinctive signals. Enlargements of the respective signals (shown in Figure S14), reveal a m/z-spacing of individual isotopic peaks which identifies the low mass signals as being caused by triply charged ions, while the high mass signals represent doubly charged ions. Simulations of the measured isotopic pattern with possible species have been performed. The measured pattern of the most abundant di- and trication matches the simulation for the respective core of the polyanion assuming formation of ion pairs between the respective polyanions and sodium counter cations that make up the charge of the ions and the complete loss of the crystal water.

Thus, the observed tri- and dications possess the general formula $\{Na_mNa_n[MO_8Pd^{II}_{12}L_8]\}^{m+}$ with m = 3 and 2. The mass shift that is observed for the different compounds corresponds to the change of the central metal **M**. In summary, the mass spectra confirm that the polyoxopalladate core remains intact in the gas phase.

The trications and to a lesser extent also the dications are accompanied toward higher masses by additional signals. In an effort to identify the origin of these signals it was found that they can be enhanced when the experimental parameters are adjusted to allow for a more gentle transfer of ions from the ESI source to the ion trap analyzer. Figure S15 shows a typical outcome of soft versus harsher ion transfer for polyanion **ScPhAs**. Unfortunately, a clear assignment is not straightforward as most of the signals are composed of widely overlapping peaks. This is partly due to the complex isotope pattern of

dx.doi.org/10.1021/ic301537n | *Inorg. Chem.* 2012, 51, 13214−13228

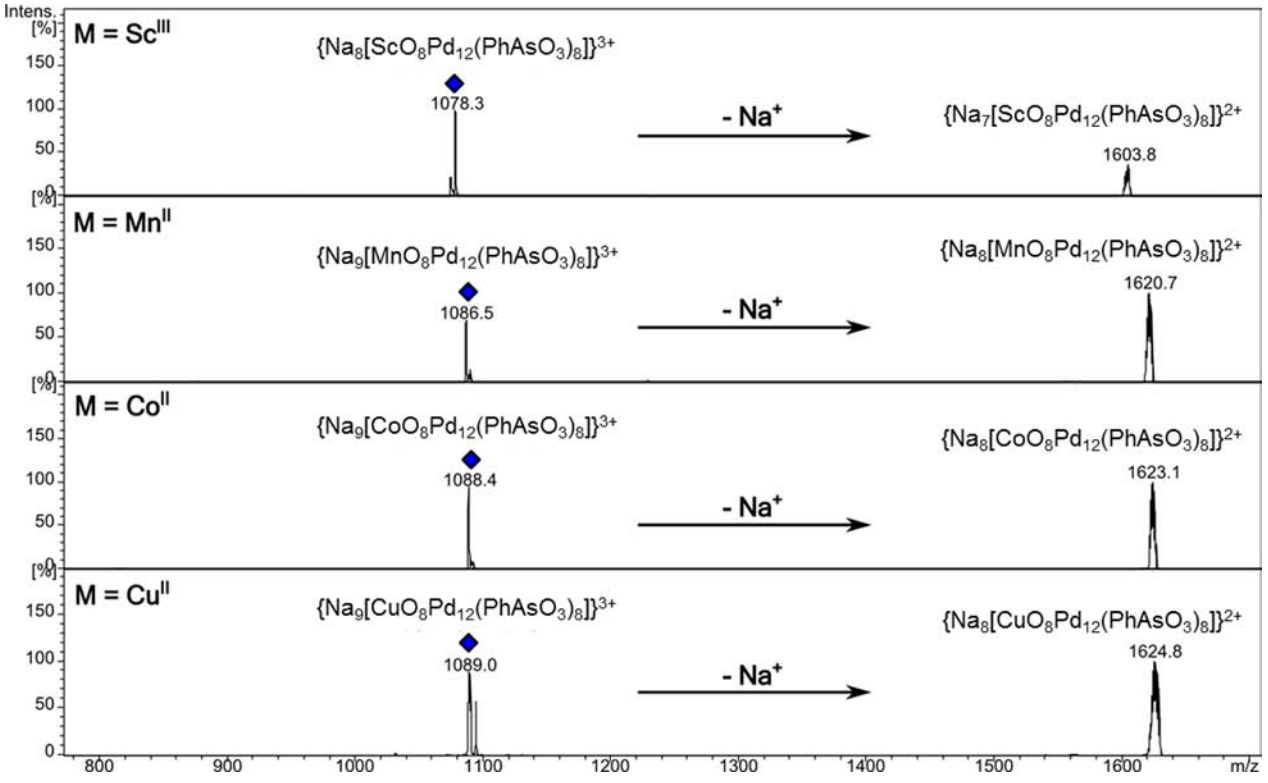

Figure 6. Collision-induced dissociations of the $\{Na_3Na_n[MO_8Pd^{2+}{}_{12}L_8]\}^{3+}$ trications with **L** = $PhAs^{V}O_3^{2-}$ and **M** = Sc^{3+}, Mn^{2+}, Co^{2+}, and Cu^{2+}.

palladium and partly caused by decomposition of larger ions into smaller ions. Therefore, we can only speculate about the nature of species associated with the polyanion core. If one assumes the likely case that H_2O is attached, the centroids of these signal bundles can be assigned to the attachment of approximately five water molecules, which may indicate enhanced stability in the present experiment. Compared with the trication, the dication shows such attachment signals to a much lesser extent. A likely explanation for this finding would be the formation of the dication by fragmentation of the trication after loss of the outer water shell. Strong support for this fragmentation mechanism is obtained in so-called MS/MS experiments by means of collision-induced dissociation (CID). The bare trications were isolated as precursor ions and underwent controlled collisions with helium atoms in the quadrupole ion trap.

The resulting MS/MS spectra are shown in Figure 6. The triply charged precursor ion (marked with a diamond) undergoes a dissociation which is known as Coulomb explosion in which the multiply charged precursor dissociates by charge separation. In the present case, the $\{Na_3Na_n[MO_8Pd^{II}{}_{12}L_8]\}^{3+}$ trications dissociate into $\{Na_2Na_n[MO_8Pd^{II}{}_{12}L_8]\}^{2+}$ dication and Na^+, the mass of which is too low to allow its detection in the used ion trap mass spectrometer. The MS/MS experiments confirm the identity of the trications and dications and establish their relationship as precursor and fragment ion.

Magnetic Studies. The availability of some paramagnetic ions in the rather rare 8-fold coordination provided an opportunity to study their ground state electronic properties using high-frequency EPR (HF-EPR). Detailed HF-EPR measurements studies were made on **Na-MnPhAs** and **Na-CuPhAs**. Figure 7 shows typical HF-EPR spectra of **Na-MnPhAs** taken at the very high frequency of 406.5 GHz and at various temperatures ranging from 290 K down to 4.5 K.

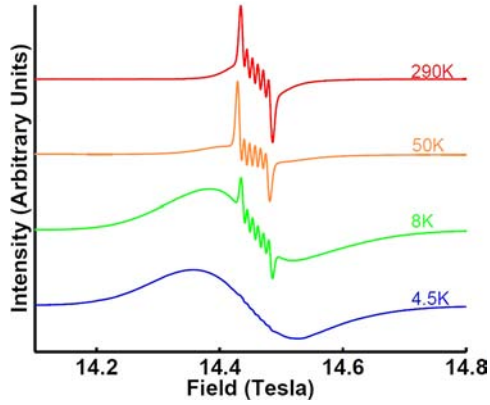

Figure 7. 406.5 GHz EPR spectra of **Na-MnPhAs** at different temperatures as indicated. At high fields and low temperature the sharp features due to the $m_S = -1/2$ to $m_S = +1/2$ transition disappear due to the negligible population. At the lowest temperature only the $m_S = -5/2$ to $m_S = -3/2$ transition contributes, which is broadened due to a distribution of zero-field splitting parameters (D-strain), see text.

The main feature of these spectra at temperatures higher than 50 K is the sextet of peaks centered at a *g*-value close to 2.00, with an equal spacing of about 85 G between the individual sextet lines. This is a confirmatory evidence that the ground state of the metal ion has its orbital angular momentum *L* quenched and its nuclear spin (*I*) is 5/2, identifying the metal ion as Mn^{2+} (as expected). Whereas the sharp features arise from the $m_S = -1/2$ to $m_S = +1/2$ transition of the Mn^{2+} $S = 5/2$ state, the broader features are due to the other 4 allowed transitions in this sextet. The 50 K spectrum was analyzed in more detail, using the usual spin-Hamiltonian [eq 1]:

dx.doi.org/10.1021/ic301537n | *Inorg. Chem.* 2012, 51, 13214−13228

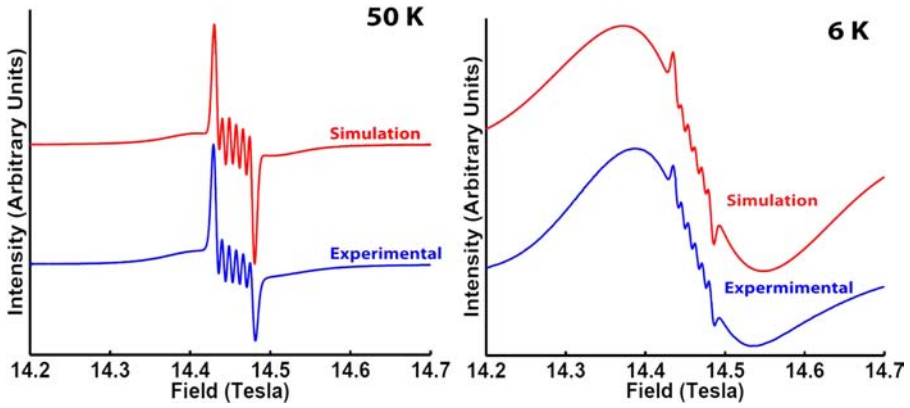

Figure 8. 406.5 GHz EPR spectra of **Na-MnPhAs** at 50 K (left) and 6 K (right).

$$\hat{H} = g\mu_B \mathbf{B}\cdot\hat{\mathbf{S}} + D(\hat{S}_z^{\,2} - \hat{\mathbf{S}}^2/3) + E(\hat{S}_x^{\,2} - \hat{S}_y^{\,2}) + A\hat{\mathbf{I}}\cdot\hat{\mathbf{S}} \quad (1)$$

where the Landé factor g and the hyperfine constant A are assumed to be isotropic, and D and E are the axial and rhombic second order zero-field splitting parameters, and the other terms have their usual meaning.[10] A standard computer fitting (Figure 8 left panel) with $S = I = 5/2$ gave the following parameters: $g = 2.0092(5)$, $A = 242(1)$ MHz (86 G), $\langle D\rangle = 0$, hence $\langle E\rangle = 0$, with a Gaussian distribution about these zero values. The average geometry of the Mn^{2+} ion at 50 K and above must thus be considered to be cubic, in agreement with the XRD analysis. On the other hand, to obtain a good fit of the low temperature spectrum, a significant distribution in the zero-field splitting must be included.

This temperature dependence of the high frequency Mn^{2+} spectra is typical of frozen (glassy) solutions of ions with half-filled d- or f- orbitals,[11] where a distribution of zero-field splitting values can be expected. In single crystals it is less common, although similar strain effects are, for example, seen in the EPR spectra of the single-molecule magnetic compound Mn_{12}-acetate,[12] where single crystals have a degree of disorder, and especially those of Mn^{2+}-doped CdSe nanoparticles.[13] In both cases the origin of the line broadening was attributed to the so-called "D-strain" phenomenon, which leads to a line-broadening for a $m_S \rightarrow m_S + 1$ transition proportional to $(2m_S + 1)\Delta D$, where ΔD is the width of the distribution of the zero-field splitting parameter D. Computer simulations using this model proved quite satisfactory, as can be noted from Figure 8. A most interesting aspect of the computer simulations was that the amount of spread in the D-value, that is, the amount of D-strain, increased rapidly with the lowering of temperature below 50 K. Whereas, for example, in the case of the Mn^{2+} impurities in CdSe nanoparticles, the spectra at all temperatures could be fitted with a single distribution width.[13] In this case, to obtain a good fit to the data at all temperatures, the D-strain needed to be reduced at higher temperatures (from 1750 MHz at 4.5 K to 1350 MHz at 50 K). At present we can only speculate that this means that the structural distortion increases markedly at lower temperatures. Further studies are in progress to unveil the mechanism of this somewhat unexpected finding, which might indicate that some dynamical effects on the time scale of the EPR experiment ($\sim 10^{-10}$–10^{-11} s) play a role.

Along the same lines, HF-EPR studies of **Na-CuPhAs** were performed to determine whether the XRD finding of a perfectly cubic environment or the theoretical work (vide infra) which predicted a distortion of the oxygen cage was correct. Figure 9

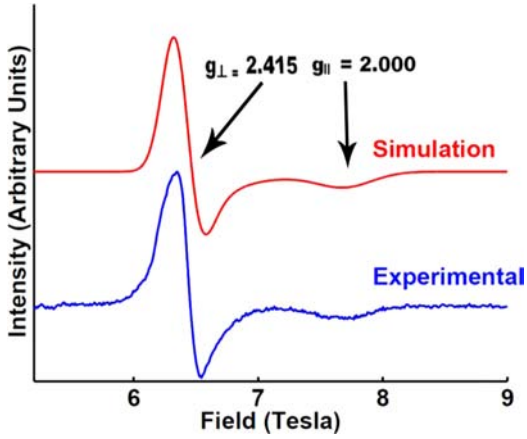

Figure 9. Typical 216 GHz EPR spectrum and simulation of **Na-CuPhAs** at 4.5 K. Two peaks are seen due to the anisotropic g-values because of a distortion from cubic to tetragonal symmetry.

shows a typical EPR spectrum of **Na-CuPhAs** at 216 GHz and 4.5 K. The fitting parameters are as follows $S = 1/2$, $g_\parallel = 2.000$, $g_\perp = 2.415$. The results confirm the theoretical work that there is in fact a distortion of the ligand environment from cubic symmetry as seen due to the asymmetric g-values. Notably, $g_\parallel < g_\perp$ is quite uncommon for most known Cu^{2+} complexes. The HF-EPR studies confirm that the distortion, due to the Jahn–Teller effect, predicted by the theoretical work was indeed correct. It is presumed that the cubic symmetry seen by XRD must be a static average.

Preliminary EPR studies were also carried out on **Na-FePhAs** and **Na-CoPhAs**. The Co^{2+}-containing sample yielded no EPR signal using high frequencies up to 406 GHz and temperature down to 4 K. The Fe^{3+}-containing sample yielded only a broad, featureless signal, and did not provide any new magnetic-structural correlation clues. The **Na-CuPhP** sample is clearly similar to **Na-CuPhAs** and hence not discussed here in detail for the sake of brevity.

Electrochemistry. We also performed the solution electrochemistry of compounds **Na-MPhAs** (M = Mn^{2+}, Fe^{3+}, Co^{2+}, Ni^{2+} and Cu^{2+}) and **Na-MSe** (M = Mn^{2+}, Fe^{3+}, Co^{2+}, Ni^{2+} and Cu^{2+}) in a pH 5 phosphate medium. For this purpose, the stabilities of the polyanions in this medium were assessed by monitoring their respective UV–visible spectra (see SI for details). A complementary cross-check of this stability was obtained by cyclic voltammetry (CV). The selected compounds have potentially electro-oxidizable (Co^{2+}, Mn^{2+}, and Pd^{2+}) and

dx.doi.org/10.1021/ic301537n | Inorg. Chem. 2012, 51, 13214–13228

electro-reducible (Fe^{3+}, Cu^{2+}, and Pd^{2+}) centers. On the other hand, Ni^{2+} is not expected to be detected under our experimental conditions, and indeed no obvious response was observed in CV that could be assigned to this cation. No voltammogram waves could be assigned to Co^{2+} or to Cu^{2+} centers with the presently studied species. This behavior is not unprecedented, and was previously reported for polyanions containing any of these metals.[3g,14] The Ni^{2+}, the Co^{2+}, and the Cu^{2+} centers gave no detectable electrochemical responses, and the overall voltammograms within each series of compounds were similar to the behavior of the Pd^{2+} centers. Hence, we concentrate on the CV of the POMs encapsulating electroactive centers, that is, Mn^{2+} and Fe^{3+}, for which the influence of the nature of the capping group is particularly pronounced, and describe the electrochemical properties of their Pd^{2+} centers. For the sake of clarity, the discussion will be divided into three parts, one concerning the central, oxidizable Mn^{2+}, another dealing with the central, reducible Fe^{3+}, and a third section devoted to Pd^{2+}.

Positive Potential Domain. At a bare glassy carbon working electrode, the Mn^{2+} in **MnPhAs** is oxidized to Mn^{3+}, the oxidation wave peaking at +0.814 V. This corresponds to a cathodic shift of just 0.016 V with respect to the oxidation wave of the related species $\mathbf{MnPd_{12}P_8}$.[3i] A striking cathodic shift of 0.170 V is observed with **MnSe** (Figure 10), which means that

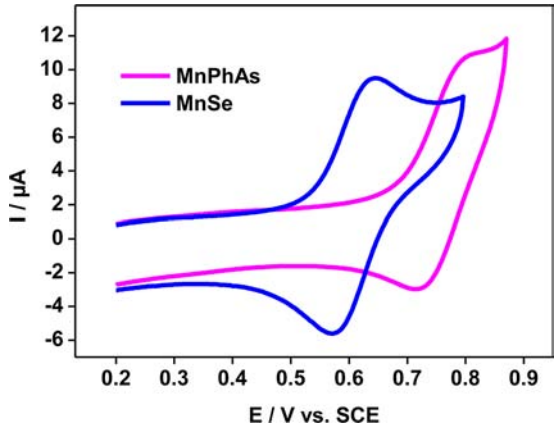

Figure 10. Comparison of the cyclic voltammograms obtained with 2 × 10^{-4} M solutions of **Na-MnPhAs** and **Na-MnSe** in 0.4 M NaH_2PO_4/NaOH, pH = 5, at 10 mV s^{-1}.

Mn^{2+} oxidation becomes easier by replacing the phenylarsonate capping groups by selenite. This trend has been confirmed by subsequent DFT calculations (vide infra) which led to an energy difference of 0.213 eV between the highest occupied molecular orbitals having a significant contribution from Mn^{2+}. Such a behavior is explained by the higher energies of the d(Mn^{2+}) orbitals when the capping group is SeO_3^{2-}. The ensemble of the results for these compounds is compiled in Table 3. These reversible processes are diffusion-controlled as revealed by the peak current dependence on the square-root of the scan rate (Figures 11 and S18). At higher potentials, other oxidation processes involving manganese and palladium take place (see Figure S19 for details).

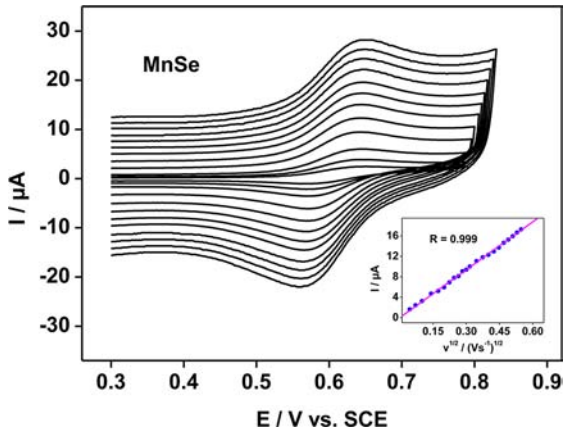

Figure 11. Cyclic voltammograms as a function of the scan rate for a 2 × 10^{-4} M solution of **Na-MnSe** in 0.4 M NaH_2PO_4/NaOH, pH = 5. Inset: anodic peak current intensity variation as a function of the square-root of the scan rate.

Still in the case of **MnSe**, the peak potentials were not influenced by the pH between 5 and 7 (Figure 12). The

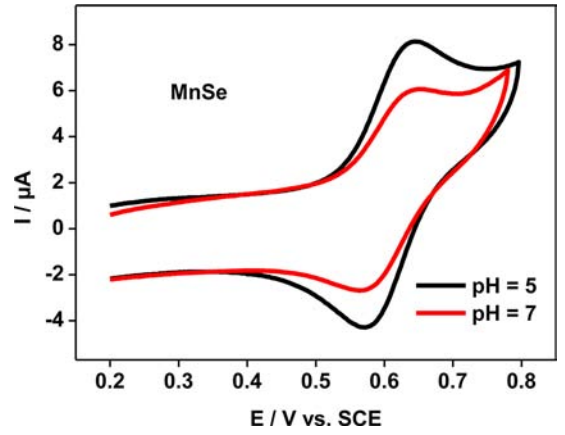

Figure 12. Comparison of the cyclic voltammograms obtained with a 2 × 10^{-4} M solution of **Na-MnSe** in 0.4 M NaH_2PO_4/NaOH, at a pH of either 5 or 7, at 10 mV s^{-1}.

Table 3. Anodic (E_a) and Cathodic (E_c) Peak Potentials and Their Shifts (ΔE_a and ΔE_c), Energy Differences between the Involved Orbitals as Determined by DFT (ΔE in eV), Peak Potential Differences ($\Delta E_p = E_a - E_c$), Formal Potentials ($E^{0\prime} = (E_a + E_c)/2$) and Formal Potential Differences ($\Delta E^{0\prime}$) for the Electron Transfer Processes Discussed in the Text[a]

	E_a	ΔE_a	E_c	ΔE_c	ΔE	ΔE_p	$E^{0\prime}$	$\Delta E^{0\prime}$
MnPhAs	+0.814					0.100	+0.764	
MnSe	+0.644	−0.170			−0.213	0.070	+0.609	−0.155
FePhAs			−0.294			0.090	−0.249	
FeSe			−0.434	−0.140	−0.140	0.104	−0.382	−0.133

[a]The experimental values are taken from voltammograms obtained at 10 mV s^{-1}. All values other than ΔE are in V vs SCE.

dx.doi.org/10.1021/ic301537n | *Inorg. Chem.* 2012, 51, 13214−13228

influence of the pH in the case of **MnPhAs** is more complex, since a response assigned to the oxidation of Pd^{2+} comes into play in the same potential range as the oxidation of Mn^{2+} at pH 7, resulting in convoluted waves.

Negative Potential Domain. In the case of Fe^{3+}, the $PhAsO_3^{2-}$ derivative **FePhAs** is reduced at −0.294 V, corresponding to a negligible anodic shift when compared to the reduction wave of $\mathbf{FePd_{12}P_8}$.[3i] A cathodic shift of 0.140 V is observed for **FeSe** when compared to **FePhAs** (Figure 13): the

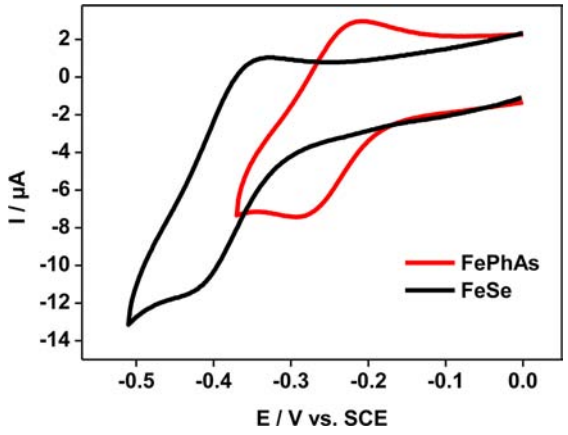

Figure 13. Comparison of the cyclic voltammograms obtained with 2 × 10^{-4} M solutions of **Na-FePhAs** and **Na-FeSe** in 0.4 M NaH_2PO_4/NaOH, pH = 5, at 10 mV s^{-1}.

reduction wave is now at −0.434 V (Table 3). A perfect match between the electrochemical result and the lowest unoccupied molecular orbital (LUMO) energy difference (0.140 eV) obtained by DFT is observed. The higher LUMO energy of **FeSe** with respect to that of **FePhAs** is due to a shorter distance observed for the M-O bonds when the capping group is SeO_3^{2-}. These reversible processes are diffusion-controlled as revealed by the peak current dependence on the square-root of the scan rate (Figure S20). The anodic to cathodic peak potential differences, ΔE_p, are 0.070 V for **MnSe**, 0.090 V for **FePhAs**, and 0.100 V both for **MnPhAs** and for **FeSe**, and they increase with the scan rate for scan rates higher than 100 mV s^{-1}. This is indicative of the presence of quasi-reversible electron transfer processes, the most reversible being the one with the smallest ΔE_p (**MnSe**), which means that electron transfer is the most favorable in this case. The magnitude of the cathodic shift when $PhAsO_3^{2-}$ is replaced by SeO_3^{2-} is slightly more important in the case of the Mn-containing species than in the Fe-containing ones, judging from the variations in the formal potential values, $\Delta E^{0\prime}$ (−0.155 vs −0.133 V, respectively). This may indicate that the effect of the replacement is more pronounced for the Mn- than for the Fe-centered electron transfer processes, in accordance with the DFT results.

The Fe-containing compounds have also been tested in pH = 7 phosphate buffer, and the peak potentials turned out to be independent of the pH (Figure S21). This behavior has already been reported before, for example for multi-iron sandwich-type POMs in the pH range 5 to 7.[15]

Pd-Related Electrochemical Features. In the negative domain, and as expected from previous work[3b,i] (see SI for details), Pd^{2+} is deposited as Pd^0 on the glassy carbon working electrode surface upon reduction (Figure S22). By and large, all compounds studied in this work lead to the formation of a palladium film on the electrode surface.

In the positive potential domain, and once a Pd^0 film has been previously formed on the electrode surface, the expected fingerprints assigned to the formation, upon oxidation, of palladium oxides and their subsequent reduction to metallic palladium, Pd^0, have been clearly observed with the present compounds (Figures S23 and S24).

The $PhAsO_3^{2-}$ derivatives are more effective for hydrogen evolution than the SeO_3^{2-} ones, in agreement with the less negative redox potentials of the former. For example, the onset for the hydrogen evolution reaction is anodically shifted by 0.070 V when **FeSe** is replaced by **FePhAs**. Following the same trend, the oxidation of Pd^{2+} is more favorable in the SeO_3^{2-} derivatives (Figure S25), in agreement with the relative positions of the highest occupied molecular orbital (HOMO) orbitals by DFT.

Theoretical Analysis. We have explored the electronic properties for the series of polyanions $[MO_8Pd^{II}_{12}L_8]^{n-}$ with **L** = $PhAsO_3^{2-}$ and **M** = Sc^{2+}, Mn^{2+}, Fe^{3+}, Cu^{2+}, and Zn^{2+}. Some preliminary calculations have also been performed for **L** = SeO_3^{2-} and **M** = Cu^{2+} and Zn^{2+}. When a metal atom is surrounded by eight oxygen atoms in a cubic arrangement, the d orbital splitting energy diagram is similar to what we find in a tetrahedral environment as shown in Figure 14. Throughout this paper we have used t_{2g} and e_g symmetry labels even though the real symmetry of the molecule is not O_h.[16]

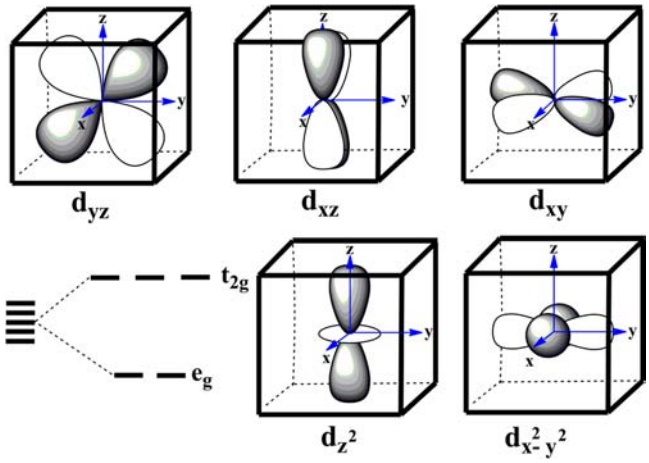

Figure 14. Orbital splitting energy diagram for a metal atom surrounded by eight ligands that occupy the vertices of a cube. The lowest energy orbitals have the lobes oriented toward the center of the cube faces.

We will initiate the discussion with the Sc^{3+} ion that has no d electrons and therefore the ground state is a singlet. For all the anions we will focus our analysis mainly on the properties of the central ion. In all systems, the computed distances are rather well reproduced, although they are found systematically somewhat longer than the experimental ones. Thus for example, the observed average metal−oxygen and oxygen−oxygen distances of the pseudocubic box in anion **ScPhAs** are 2.257 Å and 2.590 Å, whereas the computed values in aqueous solution are 2.280 Å and 2.628 Å, respectively. The distance of the 12 Pd atoms to the central atom has also been computed slightly longer than the experimental ones. It is worth mentioning that the discrepancy between X-ray and computed distances is higher when the calculations are performed in the

dx.doi.org/10.1021/ic301537n | *Inorg. Chem.* 2012, 51, 13214−13228

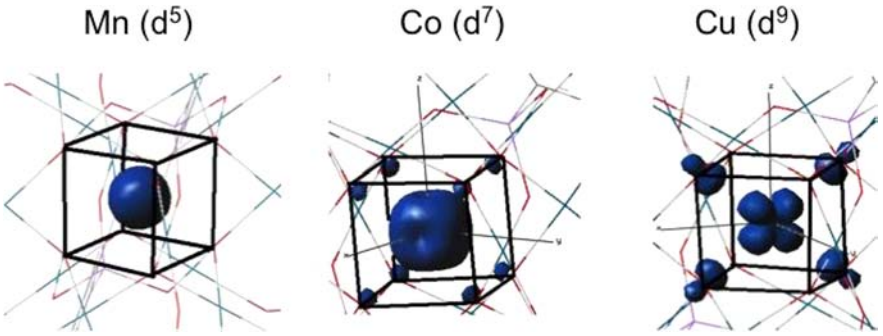

Figure 15. Spin densities determined for $[M^{II}O_8Pd^{II}_{12}(PhAs^{V}O_3)_8]^{6-}$ for **M** = Mn^{2+}, Co^{2+}, and Cu^{2+}. For **M** = Cu^{2+} the polyanion is computed to be strongly distorted with a significant delocalization of the spin density over the four closest oxygen atoms. For **M** = Mn^{2+} the spin density is spherical, according to the formal $e^2t_{2g}^3$ configuration, and strongly localized on the central ion. For **M** = Co^{2+} the smooth depressions in the pseudospherical spin density distribution can be easily rationalized from the $e^4t_{2g}^3$ configuration (see text).

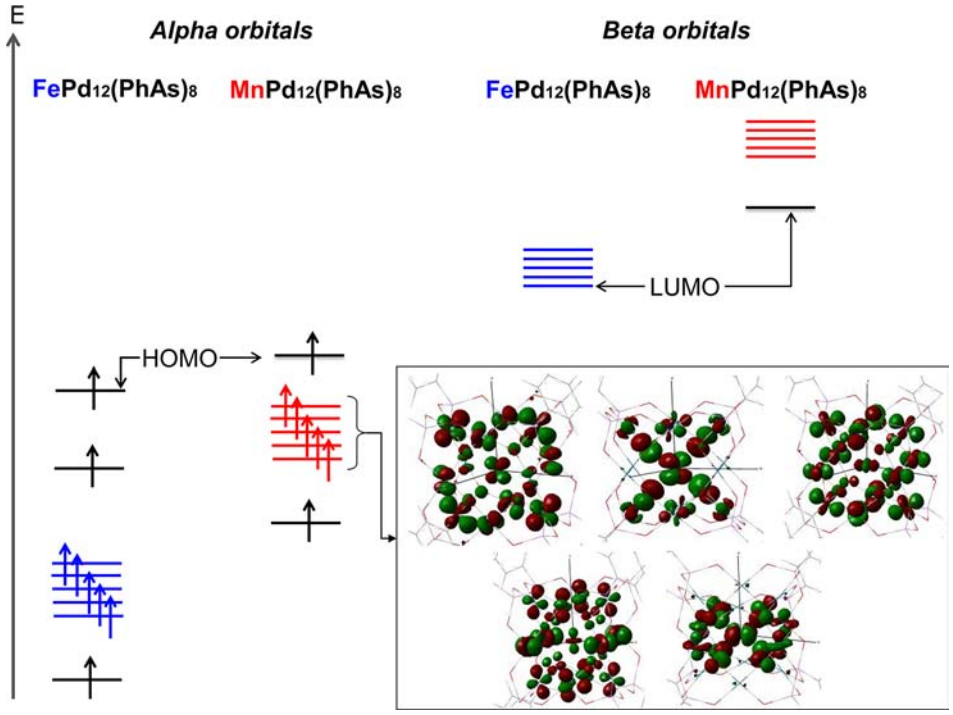

Figure 16. Frontier molecular orbital diagram for $[MO_8Pd^{II}_{12}(PhAs^{V}O_3)_8]^{n-}$ for **M** = Mn^{2+} and Fe^{3+} and representation of the five occupied orbitals with significant contribution of d(Mn) orbitals. As expected the position of Mn^{2+} (red) and Fe^{3+} (blue) orbitals are shifted differently with respect to the frontier Pd (black) orbitals. For **M** = Fe^{3+} the LUMO is an orbital with significant contribution of d(Fe) atomic orbitals, whereas for Mn^{2+} derivative the LUMO is a Pd like orbital. The figure only represents schematically the relative energy for some occupied alpha orbitals and some unoccupied beta orbitals.

gas phase. The incorporation of solvent via a polarized continuum media modifies slightly the electronic structure of the polyanion reducing the volume of the internal pseudo cubic box (see Table S6 for comparison of structures computed in the gas phase and in solution).

Anions with five d electrons (Mn^{2+} and Fe^{3+}) exhibit a richer electronic structure. A priori, we have three possible configurations: $e_g^4t_{2g}^1$, $e_g^3t_{2g}^2$, or $e_g^2t_{2g}^3$, but our DFT studies in agreement with EPR data clearly suggest that for **M** = Mn^{2+} the high spin state with five unpaired electrons is much more favorable than a configuration with four electrons residing in the e_g orbitals and one in a t_{2g}, which was found about 80 kcal·mol^{-1} higher in energy. However, more accurate energies would require an ab initio multireference treatment that is beyond the present study. According to the symmetric occupation of the five d orbitals the sextuplet ground state exhibits an almost spherical spin density, as Figure 15 shows. We note the absence of a contribution from the neighboring oxygens to the spin density, which would be a symptom of important ionic interactions between the oxo ligands and the central metal atom. In the sextuplet ground state, all eight Mn−O distances are equivalent and they were computed to be approximately 2.351 Å in aqueous solution, about 0.05 Å longer than the values observed in the solid state. No significant differences were found for the Fe^{3+}-containing derivative. We have also evaluated both high and low multiplicity states, but we could not converge the doublet state. Again, the computed geometry for the sextuplet coincides rather well with the experimental one. It is worth mentioning that the d(Fe^{3+}) orbitals (Figure 16) have been systematically found lower in energy than the equivalent orbitals for the Mn^{2+} ion, which is

dx.doi.org/10.1021/ic301537n | Inorg. Chem. 2012, 51, 13214−13228

Table 4. Relevant Distances d[a], Atomic Charges q, and Spin Densities[b] Computed for Polyanions $[MO_8Pd^{II}{}_{12}L_8]^{n-}$ (L = $PhAsO_3^{2-}$, SeO_3^{2-})

M	config.	2S + 1	$d_{(M-O)}$	$d_{(O\cdots O)}$	$d_{(M\cdots Pd)}$	q^M	q^O	spin density
ScPhAs	d^0	1	2.280 (2.257)	2.628 (2.590)	3.383 (3.310)	+2.35	−0.80	
MnPhAs	d^5	6	2.351 (2.294)	2.716 (2.662)	3.411 (3.341)	+1.48	−0.72	4.9
FePhAs	d^5	6	2.262 (2.224)	2.615 (2.561)	3.375 (3.309)	+1.66	−0.71	4.2
CoPhAs	d^7	4	2.305 (2.259)	2.663 (2.574)	3.390 (3.320)	+1.50	−0.70	2.8
CuPhAs	d^9	2	2.167/2.501 (2.270)	2.695 (2.631)	3.397/3.590 (3.327)	+1.50	−0.70	0.7
ZnPhAs	d^{10}	1	2.331 (2.269)	2.695 (2.630)	3.399 (3.329)	+1.87	−0.70	
MnSe	d^5	6	2.292/2.306 (2.219/2.261)	2.656/2.670 (2.545/2.626)	3.375/3.383 (3.292/3.326)	+2.07	−0.72	4.9
FeSe	d^5	6	2.234/2.268 (2.149/2.236)	2.578/2.581 (2.472/2.608)	3.332/3.365 (3.264/3.296)	+2.26	−0.72	4.2
CuSe	d^9	2	2.164/2.401 (2.113/2.319)	2.634/2.663 (2.648/2.659)	3.365/3.367 (3.308/3.349)	+1.90	−0.70	0.7
ZnSe	d^{10}	1	2.268/2.300 (2.180/2.250)	2.643/2.656 (2.545/2.561)	3.363/3.370 (3.283/3.306)	+1.82	−0.73	

[a]All distances are in Å, values in parentheses correspond to X-ray distances. [b]Atomic charges and spin densities have been obtained with Mulliken Population Analysis.

not unexpected if we consider the different oxidation states of the two ions.

After having analyzed the two structures containing a d^5 metal ion we will now discuss the case of the derivative encapsulating a Co^{2+} (d^7) ion for which we have found the quadruplet associated to the $e_g^4t_{2g}^3$ configuration as the ground state. As for the previous species the spin density is mainly localized on the central metal ion (2.8 e). This value and the spin density representation (Figure 15) with incipient depressions oriented to the faces of the cube, exactly where the doubly occupied e_g orbitals are pointing, clearly corroborate the proposed electronic configuration. The computed distances follow similar trends as described for the previous systems.

Finally we have studied theoretically the polyanions with Cu^{2+} (d^9) and Zn^{2+} (d^{10}) occupying the central position. In the latter, no special incidences were detected, and the optimized structure was found to be undistorted and very similar to the experimental one. As expected from a formal configuration $e_g^4t_{2g}^5$ the optimized geometry for the Cu^{2+} derivative exhibits a distorted cube. The computed d(M-O) for the doublet ground state in aqueous solution range from 2.167 Å to 2.501 Å. Apparently, there is some conflict with the X-ray structure, which suggests a pseudocubic arrangement of the eight oxygen atoms around the Cu. Many attempts have been made to obtain a less distorted structure, but in all cases we have obtained a deformed geometry that can be attributed to a first-order Jahn−Teller distortion. For example, we have frozen all Cu···Pd distances to the X-ray value 3.327 Å, but the optimization process yield a deformed structure with two subsets of M-O equal to 2.168 Å and 2.276 Å. Such a situation has been observed for **L** = SeO_3^{2-} (**CuSe**). X-ray data show (Table 2) an important distortion for polyanion **CuSe**. To evaluate if the effect of the external ligand is relevant concerning the internal distortion, we have computed the structure for anions **CuSe** and **ZnSe**. Despite the closed-shell nature of Zn^{2+}, both DFT and X-ray data show a slightly distorted cube for the MO_8 unit (Table 4). In analogy to **L** = $PhAsO_3^{2-}$ the computed distances are somewhat longer than the experimental ones. For anion **CuSe** the distortion is much more important than for **ZnSe**, as in addition to the effect of the external ligand, the unsymmetrical orbital occupation for the pseudo t_{2g} orbitals of the Cu^{2+} ion clearly enforces a distorted coordination geometry for the metal ion, as shown by DFT and X-ray distances (Table 4). It is worth mentioning that when a Cu^{2+} ion occupies the central position of the polyanion, the interaction between the metal ion and the closest oxygen atoms is less ionic, as emphasized by the spin density, which is more delocalized among the oxygen atoms (Figure 15). Present DFT calculations carried out in solution are in agreement with the interpretation of the EPR data, as already mentioned above.

To substantiate the electrochemical data in Table 3 we have depicted the frontier orbitals for polyanions $[M^{II/III}O_8Pd^{II}{}_{12}(PhAsO_3)_8]^{n-}$ (**M** = Fe^{3+}, Mn^{2+}) and $[M^{II/III}O_8Pd^{II}{}_{12}(SeO_3)_8]^{n-}$ (**M** = Fe^{3+}, Mn^{2+}) in Figures S16 and S17, respectively. The largest reduction potential observed for **FeSe** can be easily rationalized from the highest energy orbital of the LUMO, which originates in the shortest distance observed for M-O bonds when the capping ligand is SeO_3^{2-}. For similar reasons, the differences in the oxidation potentials observed for the two ligands SeO_3^{2-} and $PhAsO_3^{2-}$ can be explained from the relative energies of d(Mn) occupied orbitals (in red in Figure S17). It is worth mentioning that for these polyoxopalladates the HOMO is an orbital with participation of atomic orbitals of the Pd_{12} core. Apparently, this is in contrast to the experimental electrochemical results, which allow assigning the first oxidation peak to the Mn^{2+} center. However, the reader should be aware that molecular orbitals provide just a qualitative perspective of oxidation/reduction processes and this is still more valid for open shell systems. A more accurate analysis would require studying oxidized and reduced systems. A wider discussion of the electronic properties of the novel family of polypalladates, which are very different from classical POMs,[17] will be published elsewhere.[18]

EXPERIMENTAL SECTION

Materials and Physical Measurements. All reagents were purchased from commercial sources and used without further purification. $[Pd_3(CH_3COO)_6]$ was obtained from Johnson Matthey PLC. The IR spectra of the hydrated sodium salts of **MPhAs**, **MPhP**, and **MSe** were recorded on KBr disks using a Nicolet-Avatar 370 spectrometer between 400 and 4000 cm^{-1}. Thermogravimetric analyses were carried out on a TA Instruments SDT Q600 thermobalance with a 100 mL min^{-1} flow of nitrogen; the temperature was ramped from 20 to 1200 °C at a rate of 5 °C min^{-1}. Elemental analyses were performed by Analytische Laboratorien, Lindlar (Germany) for **Na-ScPhAs** and **Na-CuPhAs**, and by Service Central d'Analyze, Solaize, France, for all the other compounds. The NMR spectra of the obtained compounds were recorded on a 400 MHz JEOL ECX instrument at room temperature using 5 mm tubes for ^1H, ^{13}C ^{31}P and ^{77}Se. The respective resonance frequencies were 399.78 MHz (^1H), 100.71 MHz (^{13}C), 162.14 MHz (^{31}P), and 76.39 MHz (^{77}Se). The chemical shifts are reported with respect to the references $Si(CH_3)_4$ (^1H and ^{13}C), 85% H_3PO_4 (^{31}P) and H_2SeO_3 (^{77}Se, δ = 1302 ppm).

dx.doi.org/10.1021/ic301537n | Inorg. Chem. 2012, 51, 13214−13228

$Na_5[Sc^{III}O_8Pd^{II}_{12}(PhAs^{V}O_3)_8]\cdot 21H_2O$ (Na-ScPhAs). [$Pd_3(CH_3COO)_6$] (0.140 g, 0.208 mmol), $PhAsO_3H_2$ (0.125 g, 0.619 mmol), and $Sc(CF_3SO_3)_3$ (0.154 g, 0.313 mmol) were dissolved in 5 mL of sodium acetate solution 1.0 M (pH 6.9). While stirring, the solution was heated to 80 °C for 90 min. Then it was cooled to room temperature, filtered and allowed to crystallize at room temperature. Dark red-brown crystals were obtained after several days, filtered off, and air-dried. Yield: 0.030 g (16% based on Pd). Elemental analysis (%) calcd: Na 3.24, Sc 1.27, As 16.91, C 16.27, H 2.33; found: Na 4.17, Sc 1.11, As 16.17, C 16.90, H 2.52. IR (2% KBr pellet, ν/cm^{-1}): 1623(m), 1479(w), 1438(m), 1178(w), 1094(m), 1026(w), 804(s), 742(s), 695(s), 629(s), 538(s), 502(sh), 435(s). NMR (ppm): ^1H, δ 7.58 (d, 2H), 7.52 (m, 1H), 7.42 (m, 2H); $^{13}C\{^1H\}$, δ 133.1 (1C), 130.8 (2C), 129.5 (2C), 126.8 (1C).

$Na_6[Mn^{II}O_8Pd^{II}_{12}(PhAs^{V}O_3)_8]\cdot 27H_2O$ (Na-MnPhAs). The compound was prepared by exactly the same procedure as **Na-ScPhAs**, but with $MnCl_2\cdot 4H_2O$ (0.031 g, 0.157 mmol) instead of $Sc(CF_3SO_3)_3$. Dark red-brown crystals were obtained. Yield: 0.060 g (32% based on Pd). Elemental analysis (%) calcd: Na 3.74, Mn 1.49, Pd 34.66, As 16.27, C 15.65, H 2.57; found: Na 3.62, Mn 1.45, Pd 33.75, As 15.90, C 16.27, H 2.02. IR (2% KBr pellet, ν/cm^{-1}): 1626(m), 1478(w), 1438(m), 1177(w), 1094(m), 1026(w), 805(s), 744(s), 695(s), 627(s), 532(s), 502(sh), 435(sh).

$Na_5[Fe^{III}O_8Pd^{II}_{12}(PhAs^{V}O_3)_8]\cdot 23H_2O$ (Na-FePhAs). The compound was prepared by exactly the same procedure as **Na-ScPhAs**, but with $Fe(NO_3)_3\cdot 9H_2O$ (0.063 g, 0.156 mmol) instead of $Sc(CF_3SO_3)_3$. Dark red-brown crystals were obtained. Yield: 0.120 g (65% based on Pd). Elemental analysis (%) calcd: Na 3.20, Fe 1.56, Pd 35.57, As 16.69, C 16.06, H 2.41; found: Na 3.22, Fe 1.52, Pd 34.61, As 16.62, C 16.53, H 2.11. IR (2% KBr pellet, ν/cm^{-1}): 1626(m), 1479(w), 1438(m), 1176(w), 1095(m), 1022(w), 804(s), 744(s), 693(s), 641(s), 538(s), 499(sh), 434(s).

$Na_6[Co^{II}O_8Pd^{II}_{12}(PhAs^{V}O_3)_8]\cdot 26H_2O$ (Na-CoPhAs). The compound was prepared by exactly the same procedure as **Na-ScPhAs**, but with $Co(NO)_3\cdot 6H_2O$ (0.058 g, 0.156 mmol) instead of $Sc(CF_3SO_3)_3$. Dark red-brown crystals were obtained. Yield: 0.130 g (69% based on Pd). Elemental analysis (%) calcd: Na 3.76, Co 1.61, Pd 34.79, As 16.33, C 15.71, H 2.53; found: Na 3.55, Co 1.50, Pd 33.96, As 16.08, C 16.44, H 2.02. IR (2% KBr pellet, ν/cm^{-1}): 1626(m), 1479(w), 1438(m), 1176(w), 1094(m), 1022(w), 807(s), 743(s), 695(s), 638(s), 613(sh), 531(s), 431(sh).

$Na_6[Ni^{II}O_8Pd^{II}_{12}(PhAs^{V}O_3)_8]\cdot 30H_2O$ (Na-NiPhAs). The compound was prepared by exactly the same procedure as **Na-ScPhAs**, but with $NiSO_4\cdot 6H_2O$ (0.055 g, 0.156 mmol) instead of $Sc(CF_3SO_3)_3$. Dark red-brown crystals were obtained. Yield: 0.125 g (65% based on Pd). Elemental analysis (%) calcd: Na 3.69, Ni 1.57, Pd 34.12, As 16.02, C 15.41, H 2.69; found: Na 3.82, Ni 1.56, Pd 33.20, As 15.78, C 16.69, H 2.04. IR (2% KBr pellet, ν/cm^{-1}): 1624(m), 1480(w), 1438(m), 1178(w), 1093(m), 1024(w), 806(s), 741(s), 692(s), 679(sh), 626(s), 592(sh), 529(s), 493(sh), 435(sh).

$Na_6[Cu^{II}O_8Pd^{II}_{12}(PhAs^{V}O_3)_8]\cdot 19H_2O$ (Na-CuPhAs). The compound was prepared by exactly the same procedure as **Na-ScPhAs**, but with $Cu(CH_3COO)_2\cdot H_2O$ (0.059 g, 0.156 mmol) instead of $Sc(CF_3SO_3)_3$. Dark red-brown crystals were obtained. Yield: 0.095 g (52% based on Pd). Elemental analysis (%) calcd: Na 4.01, Cu 1.85, As 17.42, C 16.76, H 1.93; found: Na 3.89, Cu 2.37, As 16.89, C 16.85, H 2.30. IR (2% KBr pellet, ν/cm^{-1}): 1622(m), 1478(w), 1437(m), 1176(w), 1091(m), 1022(w), 804(s), 744(s), 694(s), 647(s), 630(sh), 531(s), 501(sh), 448(sh).

$Na_6[Zn^{II}O_8Pd^{II}_{12}(PhAs^{V}O_3)_8]\cdot 37H_2O$ (Na-ZnPhAs). The compound was prepared by exactly the same procedure as **Na-ScPhAs**, but with $ZnCl_2$ (0.021 g, 0.156 mmol) instead of $Sc(CF_3SO_3)_3$. Dark red-brown crystals were obtained. Yield: 0.080 g (41% based on Pd). Elemental analysis (%) calcd: Na 3.56, Zn 1.69, As 15.47, C 14.88, H 2.97; found: Na 3.68, Zn 1.65, As 15.66, C 13.88, H 2.09. IR (2% KBr pellet, ν/cm^{-1}): 1626(m), 1482(w), 1438(m), 1180(w), 1093(m), 1024(w), 803(s), 744(s), 696(s), 641(s), 529(s), 431(sh). NMR (ppm): ^1H, δ 7.58 (d, 2H), 7.49 (m, 1H), 7.40 (m, 2H); $^{13}C\{^1H\}$, δ 132.7 (1C), 130.7 (2C), 129.2 (2C), 128.7 (1C).

$Na_6[Cu^{II}O_8Pd^{II}_{12}(PhP^{V}O_3)_8]\cdot 35H_2O$ (Na-CuPhP). [$Pd_3(CH_3COO)_6$] (0.140 g, 0.208 mmol), $PhPO_3H_2$ (0.100 g, 0.633 mmol), and $Cu(CH_3COO)_2\cdot H_2O$ (0.010 g, 0.052 mmol) were dissolved in 5 mL of 0.5 M sodium acetate solution (pH 8.0). The resulting solution was stirred and heated to 80 °C for 1 h. During the first 30 min the pH value of the reaction mixture was controlled and adjusted in the range 7.9−8.1 by adding 1 M NaOH. Then it was cooled to room temperature, filtered, and allowed to crystallize at room temperature. Red crystals were obtained after several days, filtered off, and air-dried. Yield: 0.030 g (17% based on Pd). Elemental analysis (%) calcd: Na 3.96, Cu 1.82, Pd 36.64, P 7.11, C 16.54; found: Na 4.09, Cu 1.86, Pd 37.26, P 7.23, C 15.85. IR (2% KBr pellet, ν/cm^{-1}): 1630(m), 1482(w), 1436(m), 1130(m), 1039(s), 940(s), 759(m), 718(s), 702(m), 659(sh), 606(s), 549(m).

$Na_6[Zn^{II}O_8Pd^{II}_{12}(PhP^{V}O_3)_8]\cdot 36H_2O$ (Na-ZnPhP). [$Pd_3(CH_3COO)_6$] (0.140 g, 0.208 mmol), $PhPO_3H_2$ (0.100 g, 0.633 mmol), and $ZnCl_2$ (0.0071 g, 0.052 mmol) were dissolved in 5 mL of 2.0 M sodium acetate solution (pH 8.0). The resulting solution was stirred and heated to 80 °C for 1 h. During the first 30 min the pH value of the reaction mixture was controlled and adjusted in the range 7.9−8.1 by adding 1 M NaOH. Then it was cooled to room temperature, filtered, and allowed to crystallize at room temperature. Red crystals were obtained after several days, filtered off, and air-dried. Yield: 0.030 g (17% based on Pd). Elemental analysis (%) calcd: Na 3.93, Zn 1.87, Pd 36.43, P 7.07, C 16.45; found: Na 3.93, Zn 1.86, Pd 35.79, P 6.88, C 16.25. IR (2% KBr pellet, ν/cm^{-1}): 1629(m), 1484(w), 1436(m), 1129(m), 1035(s), 939(s), 816(w), 760(m), 720(m), 701(m), 657(m), 607(s), 550(m), 445(m). NMR (ppm): ^{31}P, δ 29.5; ^1H, δ 7.53 (m, 2H), 7.37 (t, 1H), 7.30 (m, 2H); $^{13}C\{^1H\}$, δ 131.1 (s, 1C), 130.8 (d, 2C), 128.9 (s, 1C), 128.2 (d, 2C).

$Na_6[Mn^{II}O_8Pd^{II}_{12}(Se^{IV}O_3)_8]\cdot 11H_2O$ (Na-MnSe). [$Pd_3(CH_3COO)_6$] (0.140 g, 0.208 mmol), SeO_2 (0.070 g, 0.630 mmol), and $MnSO_4\cdot H_2O$ (0.009 g, 0.052 mmol) were dissolved in 5 mL of 0.5 M NaOAc solution (pH 6.9), while stirring and heating to 80 °C. After 30 min of heating the pH was adjusted to 6.4 by adding several drops of 1 M NaOH. Then the reaction mixture was heated with stirring for 1 h. The solution was cooled to room temperature and filtered. The filtrate was kept at room temperature for several days to produce red crystals, which were isolated by filtration, and air-dried. Yield: 0.040 g (28% based on Pd). Elemental analysis (%) calcd: Na 4.91, Mn 1.95, Se 22.47, Pd 45.4; found: Na 4.97, Mn 2.04, Se 22.20, Pd 45.6. IR (2% KBr pellet, ν/cm^{-1}): 1632(m), 797(s), 734(s), 645(s), 613(sh), 548(s), 501(sh).

$Na_5[Fe^{III}O_8Pd^{II}_{12}(Se^{IV}O_3)_8]\cdot 13H_2O$ (Na-FeSe). [$Pd_3(CH_3COO)_6$] (0.140 g, 0.208 mmol), SeO_2 (0.070 g, 0.630 mmol), and $Fe(NO_3)_3\cdot 9H_2O$ (0.022 g, 0.052 mmol) were dissolved in 5 mL of 0.5 M NaOAc solution (pH 6.9), while stirring and heating to 80 °C. After 10 and 30 min of heating the pH was adjusted to 6.4 by adding several drops of 1 M NaOH. Then the reaction mixture was heated with stirring for 1 h. The solution was cooled to room temperature and filtrated. The filtrate was kept at room temperature for several days to produce dark-red crystals, which were isolated by filtration, and air-dried. Yield: 0.030 g (21% based on Pd). Elemental analysis (%) calcd: Na 4.07, Fe 1.98, Se 22.35, Pd 45.19; found: Na 3.84, Fe 1.95, Se 22.40, Pd 45.21. IR (2% KBr pellet, ν/cm^{-1}): 1630(m), 797(s), 726(s), 654(s), 615(sh), 551(s), 501(sh).

$Na_6[Co^{II}O_8Pd^{II}_{12}(Se^{IV}O_3)_8]\cdot 10H_2O$ (Na-CoSe). The compound was prepared by exactly the same procedure as **Na-MnSe**, but with $Co(NO_3)_2\cdot 6H_2O$ (0.016 g, 0.052 mmol) instead of $MnSO_4\cdot H_2O$. Yield: 0.096 g (67% based on Pd). Elemental analysis (%) calcd: Na 4.93, Co 2.11, Se 22.58, Pd 45.7; found: Na 5.07, Co 2.14, Se 21.75, Pd 46.3. IR (2% KBr pellet, ν/cm^{-1}): 1628(m), 799(s), 738(s), 658(s), 624(sh), 548(s), 505(sh).

$Na_6[Ni^{II}O_8Pd^{II}_{12}(Se^{IV}O_3)_8]\cdot 11H_2O$ (Na-NiSe). The compound was prepared by exactly the same procedure as **Na-FeSe**, but with $NiSO_4\cdot 6H_2O$ (0.014 g, 0.052 mmol) instead of $Fe(NO_3)_3\cdot 9H_2O$. Yield: 0.068 g (47% based on Pd). Elemental analysis (%) calcd: Ni 2.08, Na 4.90, Pd 45.36, Se 22.44; found: Ni 1.97, Na 4.89, Pd 45.49, Se 22.62. IR (2% KBr pellet, ν/cm^{-1}): 1629(m), 800(s), 732(s), 654(s), 615(sh), 548(s), 510(sh).

$Na_6[Cu^{II}O_8Pd^{II}_{12}(Se^{IV}O_3)_8]\cdot 12H_2O$ (Na-CuSe). The compound was prepared by exactly the same procedure as **Na-MnSe**, but with $Cu(CH_3COO)_2\cdot H_2O$ (0.011 g, 0.052 mmol) instead of $MnSO_4\cdot H_2O$. Yield: 0.100 g (70% based on Pd). IR (2% KBr pellet, ν/cm^{-1}): 1617(m), 797(s), 725(s), 666(sh), 611(sh), 546(s). Elemental analysis (%) calcd: Cu 2.24, Na 4.86, Pd 45.0, Se 22.26; found: Cu 2.15, Na 4.78, Pd 44.6, Se 22.40.

$Na_6[Zn^{II}O_8Pd^{II}_{12}(Se^{IV}O_3)_8]\cdot 13H_2O$ (Na-ZnSe). The compound was prepared by exactly the same procedure as **Na-MnSe**, but with $ZnCl_2$ (0.007 g, 0.052 mmol) instead of $MnSO_4\cdot H_2O$. Yield: 0.113 g (79% based on Pd). Elemental analysis (%) calcd: Zn 2.29, Na 4.83, Pd 44.7, Se 22.10; found: Zn 2.78, Na 5.09, Pd 44.4, Se 22.51. IR (2% KBr pellet, ν/cm^{-1}): 1628(m), 797(s), 737(s), 656(s), 624(sh), 547(s), 506(sh). NMR (ppm): ^{77}Se, δ 1222.5.

$Na_5[Lu^{III}O_8Pd^{II}_{12}(Se^{IV}O_3)_8]\cdot 10H_2O$ (Na-LuSe). The compound was prepared by exactly the same procedure as **Na-MnSe**, but with $LuCl_3\cdot 6H_2O$ (0.020 g, 0.052 mmol) instead of $MnSO_4\cdot H_2O$. Yield: 0.078 g (52% based on Pd). Elemental analysis (%) calcd: Lu 6.05, Na 3.98, Pd 44.2, Se 21.85; found: Lu 5.96, Na 4.19, Pd 44.3, Se 19.74. IR (2% KBr pellet, ν/cm^{-1}): 1628(m), 793(s), 723(s), 629(s), 552(s), 435(m). NMR (ppm): ^{77}Se, δ 1223.8.

X-ray Crystallography. Data for the structures of **Na-MPhAs**, **Na-MPhP**, and **Na-MSe** were collected on a Bruker Kappa X8 APEX CCD single-crystal diffractometer equipped with a sealed Mo tube and graphite monochromator (λ = 0.71073 Å). Crystals were mounted either in Hampton cryoloop with light oil (for **Na-MPhAs**, **Na-MPhP**, and **Na-MSe** (M = Co^{2+}, Ni^{2+}, Cu^{2+} and Lu^{3+}) at 100 or 173 K, see Tables S1−S5 for details) or on a glass fiber in epoxy glue (for **Na-MnSe**, **Na-FeSe**, and **Na-ZnSe** at room temperature) to prevent water loss. The SHELX software package (Bruker) was used to solve and refine the structures.[19] Absorption corrections were applied empirically using the SADABS program.[20] The structures were solved by direct methods and refined by the full-matrix least-squares method minimization of $(\sum w(F_o - F_c)^2)$ with anisotropic thermal parameters for all heavy POM skeleton atoms (**M**, Pd, As, P, Se) and some sodium countercations. The hydrogen atoms of the phenyl rings in **Na-MPhAs** and **Na-MPhP** were introduced in geometrically calculated positions. The H atoms of the crystal waters were not located in any of the compounds. The relative site occupancy factors for the disordered positions of sodium atoms and oxygen atoms of crystallization water molecules were refined in an isotropic approximation and then fixed at the obtained values.

The Na counter cations in all the structures were highly disordered and all (for **Na-MPhAs** and **Na-MPhP**) or partially (**Na-MSe**; M = Fe^{3+}, Co^{2+}, Ni^{2+}, Cu^{2+}, Zn^{2+}, Lu^{3+}) could not be located by XRD, which is a common problem in POM crystallography. The exact number of countercations and the crystal water contents in the bulk material of **Na-MPhAs**, **Na-MPhP**, and **Na-MSe** were determined by elemental analyses and TGA. The obtained formulas were then further used throughout the paper and in the CIF files for overall consistency because all further studies have been performed on the bulk material.

The high value for R_{int} on merging the data compared to R_{sigma} (0.20 cf. 0.11 for **Na-CoPhAs**, 0.24 cf. 0.11 for **Na-CuPhP**, 0.18 cf. 0.07 for **Na-CoSe**) together with several violations of systematic absences are consistent with the crystals of these compounds having at least one "friend", especially as structure solution and refinement in lower symmetry space groups (even in *P*1) did not yield an improved model. As we were unable to discern any pattern in the list of reflections for which F(obs) ≫ F(calc), we were not able to systematically remove composite reflections. Small size and poor diffraction of the crystals of **Na-MSe** (M = Mn^{2+}, Fe^{3+}, Co^{2+}, Zn^{2+}, and Lu^{3+}) at high 2θ values did not allow us to obtain data with the coverage of 2θ up to 50 degrees (see SI for details). Nevertheless, the obtained data allowed us to unambiguously locate all atoms of the POM skeleton as well as most of the counter cations and some oxygens of crystal water molecules.

Additional crystallographic data are summarized in Tables S1−S5.

Mass Spectrometry. All mass spectrometric experiments were performed with a quadrupole ion trap mass spectrometer (Bruker Esquire 6000) equipped with an electrospray ion source. The samples were prepared by dissolving the analytes in water (HPLC grade, Merck) and diluting them to a final concentration of 10^{-4} M. In the electrospray process the analyte solution was sprayed at atmospheric pressure within a potential field of 4 kV to achieve ion formation. The spray was operated with a nebulizing gas pressure (nitrogen) of 10.0 psi and a dry gas flow (nitrogen) of 5 l/min. The nebulizing and dry gas settings were in some cases altered to achieve better signal intensities; no other influence on the spectra was observed in those cases. The dry gas was heated to a temperature of 300 °C for the desolvation of the ions. After the ionization process the analyte ions entered the vacuum section and were guided by octopoles into the quadrupole ion trap for mass analysis. In MS/MS experiments an ion of interest was mass-selected inside the ion trap and by collision-induced dissociations (CID) with He (~10^{-6} mbar), a daughter ion spectrum was obtained.

Magnetic Studies. All EPR measurements were carried out using the variable frequency, high-field EPR equipment available at the National High Magnetic Field Laboratory in Tallahassee, Florida. These spectrometers have been developed locally, and reach microwave frequencies from 44 GHz to over 450 GHz, as described earlier.[21] The spectrometers use Schottky diodes/mixers and a scanable superconducting magnet that can reach 14 T. An Oxford continuous flow cryostat provided variable temperatures over the 400 K−1.3 K range, with a precision better than 0.1 K. Field calibration was achieved by using *g*-value standards. Experimental spectra were analyzed using the in-house developed computer programs and procedures as described earlier.,[3i,21,22] but with D-strain correction as described in the text.

Electrochemistry. The source, mounting, and polishing of the glassy carbon electrodes have been described.[23] Controlled potential coulometry was carried out with a large surface area glassy carbon plate. The electrochemical setup was an EG & G 273 A driven by a PC with the M270 software. Potentials are quoted against a saturated calomel electrode (SCE). The counter electrode was a platinum gauze of large surface area. The solutions for electrochemistry were deaerated thoroughly for at least 30 min with pure argon and kept under a positive pressure of this gas during the experiments. All experiments were performed at room temperature. UV−visible spectra were recorded with a Lambda 19 Perkin-Elmer spectrophotometer. POM solutions with concentrations ranging from 2×10^{-5} to 1×10^{-4} M were placed quartz cuvettes with an optical path of 2 mm. The composition of the aqueous media was 0.4 M NaH_2PO_4/NaOH, pH = 5 or 7.

Computational Details. DFT calculations were carried out with the Gaussian 09 package.[24] We used B3LYP hybrid functional[25] and the LANL2DZ pseudopotential[26] with double polarization for all the metal atoms as well as for atoms with a higher atomic number than the oxygen. For carbon and hydrogen atoms, 6-31G basis set have been used, whereas for oxygen atoms, we used the same basis set but including a polarization function.[27] All the calculations have been optimized with C_{2h} symmetry restrictions but calculations with C_1 symmetry were also performed for polyanions encapsulating Cu^{2+} and Zn^{2+}. For the open-shell systems the unrestricted level was applied. SMD implicit model[28] was used to simulate the effect of the solvent. EPR simulations were completed using the Matlab software with the EasySpin toolbox.

■ CONCLUSIONS

A large family of 16 novel polyoxopalladates $[MO_8Pd^{II}_{12}L_8]^{n-}$, (1) **L** = $PhAsO_3^{2-}$, **M** = Sc^{3+}, Mn^{2+}, Fe^{3+}, Co^{2+}, Ni^{2+}, Cu^{2+}, Zn^{2+}; (2) the first member of palladates with **L** = $PhPO_3^{2-}$, **M** = Cu^{2+}, Zn^{2+}; (3) **L** = SeO_3^{2-}, **M** = Mn^{2+}, Fe^{3+}, Co^{2+}, Ni^{2+}, Cu^{2+}, Zn^{2+}, Lu^{3+} has been prepared via facile one-pot reactions of $[Pd_3(CH_3COO)_6]$ with the appropriate capping group precursor and a salt of the heterometal ion M in aqueous sodium acetate solution. Single crystal X-ray analysis revealed a rare 8-fold coordination for the heterometal ion M incorporated in a cuboidal $\{Pd_{12}O_8L_8\}$ shell. Multinuclear ^{13}C, ^{1}H, ^{31}P, and ^{77}Se NMR studies on the diamagnetic derivatives **ScPhAs**,

dx.doi.org/10.1021/ic301537n | Inorg. Chem. 2012, 51, 13214−13228

ZnPhAs, **ZnPhP**, **ZnSe**, and **LuSe** indicate that these polyoxopalladates are stable in aqueous solution. ESI-MS confirms the identity of the polyoxopalladates in the gas phase by the detection of $\{Na_3Na_n[MO_8Pd^{II}_{12}L_8]\}^{3+}$, representing the triply sodiated core of the polyanion via ion pair formation. MS/MS studies reveal that the trications are prone to undergo a Coulomb explosion reaction into Na^+ and $\{Na_2Na_n[MO_8Pd^{II}_{12}L_8]\}^{2+}$. Electrochemistry studies showed that the central Mn^{2+} and Fe^{3+} ions give rise to reversible responses in CV. The selenite-capped polypalladates can be oxidized more easily (and are hence harder to be reduced) than their phenylarsenate-capped counterparts, a result supported by computational molecular orbital analysis at the DFT level. Hence, the Mn^{2+} oxidation wave cathodically shifts 0.170 V when going from **MnPhAs** to **MnSe**, and the reduction wave of Fe^{3+} cathodically shifts 0.140 V when going from **FeSe** to **FePhAs**. Another consequence of this shift is that the oxidation of Pd^{2+} becomes more favorable. Conversely, the phenylarsenate-capped derivatives are more efficient for reduction processes. In general, the computed structures agree very well with X-ray data, except $[Cu^{II}O_8Pd^{II}_{12}(PhAsO_3)_8]^{6-}$ for which EPR data and DFT calculations suggest a rather distorted structure in solution due to first order Jahn–Teller effects.

■ ASSOCIATED CONTENT

Supporting Information

Crystallographic data in CIF format, tables with the main crystallographic and refinement parameters (Tables S1–S5), representation of the crystal packing arrangement of **Na-MPhAs** and **Na-MPhP** (Figure S1), ^{13}C and ^{1}H NMR spectra of **ScPhAs, ZnPhAs**, and **ZnPhP** (Figures S2–S7), IR spectra (Figures S8–S10), thermograms (Figures S11–S13), mass spectra of **Na-ScPhAs** and **Na-MnPhAs** (Figures S14–S15), results of DFT calculations (Table S6, Figures S16–S17) and electrochemical studies (Figures S18–S25). This material is available free of charge via the Internet at http://pubs.acs.org.

■ AUTHOR INFORMATION

Corresponding Author

*E-mail: dalal@chem.fsu.edu (N.S.D.), u.kortz@jacobs-university.de (U.K.).

Notes

The authors declare no competing financial interest.

■ ACKNOWLEDGMENTS

U.K. and N.V.I. thank Jacobs University and the German Science Foundation (DFG-KO-2288/9-1 and DFG-IZ-60/1-1) for research support. We also acknowledge Johnson Matthey PLC for a loan of palladium(II) acetate. Dr. A. Banerjee is thanked for the registration of ^{77}Se, ^{31}P, ^{13}C, and ^{1}H NMR spectra. Figures 1, 2 and S1 were generated by Diamond Version 3.2 (copyright Crystal Impact GbR). J.M.P. thanks the Spanish Ministry of Science and Innovation (Project Nos. CTQ2011-29054-C02-01/BQU), the DGR of the Generalitat de Catalunya, (2009SGR462, and XRQTC) and the European fund for regional development, FEDER (UNRV10-4 × 10^{-1133}) for economic support. All EPR measurements were made at NHMFL, supported by NSF Cooperative Agreement No. DMR-0654118, and by the State of Florida, and DOE. P.d.O. and B.K. thank the Université Paris Sud and the Centre National de la Recherche Scientifique (CNRS) for research support.

■ DEDICATION

Dedicated to the memory of Prof. Louis Nadjo.

■ REFERENCES

(1) (a) Pope, M. T. *Heteropoly and Isopoly Oxometalates*; Springer-Verlag: Berlin, Germany, 1983. (b) Day, V. W.; Klemperer, W. G. *Science* **1985**, *228*, 533–541. (c) Pope, M. T.; Müller, A. *Angew. Chem., Int. Ed. Engl.* **1991**, *30*, 34–48. (d) *Polyoxometalates: From Platonic Solids to Antiretroviral Activity*; Pope, M. T., Müller, A., Eds.; Kluwer: Dordrecht, The Netherlands, 1994. (e) Okuhara, T.; Mizuno, N.; Misono, M. *Adv. Catal.* **1996**, *41*, 113–252. (f) *Chem. Rev.* **1998**, *98* (Special Issue on Polyoxometalates; Hill, C. L., Ed.). (g) Talismanov, S. S.; Eremenko, I. L. *Russ. Chem. Rev.* **2003**, *72*, 555–569. (h) Müller, A.; Roy, S. *Coord. Chem. Rev.* **2003**, *245*, 153–166. (i) Cronin, L. In *Comprehensive Coordination Chemistry II*; McCleverty, J. A., Meyer, T. J., Eds.; Elsevier: Amsterdam, The Netherlands, 2004; Vol. *7*. (j) Coronado, E.; Day, P. *Chem. Rev.* **2004**, *104*, 5419–5448. (k) Hill, C. L. *J. Mol. Catal. A.: Chem.* **2007**, *262*, 2–6. (l) Hasenknopf, B.; Micoine, K.; Lacote, E.; Thorimbert, S.; Malacria, M.; Thouvenot, R. *Eur. J. Inorg. Chem.* **2008**, 5001–5013. (m) Kortz, U.; Müller, A.; van Slageren, J.; Schnack, J.; Dalal, N. S.; Dressel, M. *Coord. Chem. Rev.* **2009**, *253*, 2315–2327. (n) *Eur. J. Inorg. Chem.* **2009**, *34* (Issue dedicated to Polyoxometalates; Kortz, U., Guest Ed.). (o) Long, D.-L.; Tsunashima, R.; Cronin, L. *Angew. Chem.* **2010**, *122*, 1780–1803; *Angew. Chem., Int. Ed.* **2010**, *49*, 1736–1758. (p) Putaj, P.; Lefebvre, F. *Coord. Chem. Rev.* **2011**, *255*, 1642–1685. (q) Izarova, N. V.; Pope, M. T.; Kortz, U. *Angew. Chem., Int. Ed.* **2012**, *51*, 9492–9510.

(2) (a) Sigmon, G. E.; Unruh, D. K.; Ling, J.; Weaver, B.; Ward, M.; Pressprich, L.; Simonetti, A.; Burns, P. C. *Angew. Chem.* **2009**, *121*, 2775–2778; *Angew. Chem., Int. Ed.* **2009**, *48*, 2737–2740. (b) Nicholson, B. K.; Clark, C. J.; Wright, C. E.; Telfer, S. G.; Groutso, T. *Organometallics* **2011**, *30*, 6612–6616. (c) Zhang, L.; Clérac, R.; Heijboer, P.; Schmitt, W. *Angew. Chem.* **2012**, *124*, 3062–3066; *Angew. Chem., Int. Ed.* **2012**, *51*, 3007–3011.

(3) (a) Chubarova, E. V.; Dickman, M. H.; Keita, B.; Nadjo, L.; Miserque, F.; Mifsud, M.; Arends, I. W. C. E.; Kortz, U. *Angew. Chem.* **2008**, *120*, 9685–9689; *Angew. Chem., Int. Ed.* **2008**, *47*, 9542–9546. (b) Izarova, N. V.; Dickman, M. H.; Biboum, R. N.; Keita, B.; Nadjo, L.; Ramachandran, V.; Dalal, N. S.; Kortz, U. *Inorg. Chem.* **2009**, *48*, 7504–7506. (c) Delferro, M.; Graiff, C.; Elviri, L.; Predieri, G. *Dalton Trans.* **2010**, *39*, 4479–4481. (d) Izarova, N. V.; Biboum, R. N.; Keita, B.; Mifsud, M.; Arends, I. W. C. E.; Jameson, G. B.; Kortz, U. *Dalton Trans.* **2009**, *43*, 9385–9387. (e) Xu, F.; Scullion, R. A.; Yan, J.; Miras, H. N.; Busche, C.; Scandurra, A.; Pignataro, B.; Long, D.; Cronin, L. *J. Am. Chem. Soc.* **2011**, *133*, 4684–4686. (f) Izarova, N. V.; Vankova, N.; Banerjee, A.; Jameson, G. B.; Heine, T.; Schinle, F.; Hampe, O.; Kortz, U. *Angew. Chem.* **2010**, *122*, 7975–7980; *Angew. Chem., Int. Ed.* **2010**, *49*, 7807–7811. (g) Barsukova-Stuckart, M.; Izarova, N. V.; Jameson, G. B.; Ramachandran, V.; Wang, Z.; van Tol, J.; Dalal, N. S.; Ngo Biboum, R.; Keita, B.; Nadjo, L.; Kortz, U. *Angew. Chem.* **2011**, *123*, 2688–2692; *Angew. Chem., Int. Ed.* **2011**, *50*, 2639–2642. (h) Barsukova, M.; Izarova, N. V.; Ngo Biboum, R.; Keita, B.; Nadjo, L.; Ramachandran, V.; Dalal, N. S.; Antonova, N. S.; Carbó, J. J.; Poblet, J. M.; Kortz, U. *Chem.—Eur. J.* **2010**, *16*, 9076–9085. (i) Barsukova-Stuckart, M.; Izarova, N. V.; Barrett, R.; Wang, Z.; van Tol, J.; Kroto, H. W.; Dalal, N. S.; Keita, B.; Heller, D.; Kortz, U. *Chem.—Eur. J.* **2012**, *18*, 6167–6171. (j) Xu, F.; Miras, H. N.; Scullion, R. A.; Long, D.-L.; Thiel, J.; Cronin, L. *Proc. Natl. Acad. Sci. U.S.A.* **2012**, *109*, 11609–11612. (k) Lin, Z.-G.; Wang, B.; Cao, J.; Chen, B.-K.; Gao, Y.-Z.; Chi, Y.-N.; Xu, C.; Huang, X.-Q.; Han, R.-D.; Su, S.-Y.; Hu, C.-W. *Inorg. Chem.* **2012**, *51*, 4435–4437.

(4) (a) Pley, M.; Wickleder, M. S. *Angew. Chem.* **2004**, *116*, 4262–4264; *Angew. Chem., Int. Ed.* **2004**, *43*, 4168–4170. (b) Pley, M.; Wickleder, M. S. *Z. Naturforsch. B* **2006**, *61*, 912–915.

(5) (a) Izarova, N. V.; Vankova, N.; Heine, T.; Ngo Biboum, R.; Keita, B.; Nadjo, L.; Kortz, U. *Angew. Chem.* **2010**, *122*, 1930–1933. (b) Xiang, Y.; Izarova, N. V.; Schinle, F.; Hampe, O.; Keita, B.; Kortz, U. *Chem. Commun.* **2012**, *48*, 9849–9851.

(6) (a) Pham, N. T. S.; Van Der Sluys, M.; Jones, C. W. *Adv. Synth. Catal.* **2006**, *348*, 609−679. (b) Goloboy, J. C.; Klemperer, W. G. *Angew. Chem., Int. Ed.* **2009**, *48*, 3562−3564.
(7) (a) Bergman, J. G.; Cotton, F. A. *Inorg. Chem.* **1966**, *5*, 1208−1213. (b) Bodner, R. L.; Hendricker, D. G. *Inorg. Chem.* **1973**, *12*, 33−37. (c) Christmas, C.; Vincent, J. B.; Huffman, J. C.; Christou, G.; Chang, H.-R.; Hendrickson, D. N. *Angew. Chem., Int. Ed. Engl.* **1987**, *26*, 915−916. (d) Hagen, K. S. *Angew. Chem., Int. Ed. Engl.* **1992**, *31*, 764−766. (e) Koch, W. O.; Barbieri, A.; Grodzicki, M.; Schünemann, V.; Trautwein, A. X.; Krüger, H.-J. *Angew. Chem., Int. Ed. Engl.* **1996**, *35*, 422−424. (f) Koch, W. O.; Kaiser, J. T.; Krüger, H.-J. *Chem. Commun.* **1997**, 2237−2238. (g) Louloudi, M.; Nastopoulos, V.; Gourbatsis, S.; Perlepes, S. P.; Hadjiliadis, N. *Inorg. Chem. Commun.* **1999**, *2*, 479−483. (h) Ako, A. M.; Hewitt, I. J.; Mereacre, V.; Clérac, R.; Wernsdorfer, W.; Anson, C. E.; Powell, A. K. *Angew. Chem., Int. Ed.* **2006**, *45*, 4926−4929. (i) Moreno, Y.; Hermosilla, P.; Garland, M. T.; Peña, O.; Baggio, R. *Acta Crystallogr.* **2006**, *C62*, m404−m406. (j) Nayak, S.; Lan, Y.; Clérac, R.; Anson, C. E.; Powell, A. K. *Chem. Commun.* **2008**, 5698−5700. (k) Ge, C.-H.; Ni, Z.-H.; Liu, C.-M.; Cui, A.-L.; Zhang, D.-Q.; Kou, H.-Z. *Inorg. Chem. Commun.* **2008**, *11*, 675−677. (l) Stamatatos, T. C.; Vinslava, A.; Abboud, K. A.; Christou, G. *Chem. Commun.* **2009**, 2839−2841. (m) Patra, A. K.; Dube, K. S.; Papaefthymiou, G. C.; Conradie, J.; Ghosh, A.; Harrop, T. C. *Inorg. Chem.* **2010**, *49*, 2032−2034.
(8) (a) Nishio, M.; Hirota, M.; Umezawa, Y. *The CH/pi Interaction. Evidence, Nature, and Consequences*; Wiley-VCH: New York, 1998. (b) Nishio, M. *CrystEngComm* **2004**, *6*, 130−158.
(9) Nakamoto, K. *Infrared and Raman Spectra of Inorganic and Coordination Compounds- Part A: Theory and Applications in Inorganic Chemistry*, 5th ed.; Wiley and Sons: New York, 1997.
(10) Weil, J. A.; Bolton, J. R. *Electron Paramagnetic Resonance-Elementary Theory and Practical Applications*, 2nd ed.; Wiley−Interscience: Hoboken, NJ, 2007.
(11) (a) Un, S.; Sedoud, A. *Appl. Magn. Reson.* **2010**, *37*, 247. (b) Angerhofer, A.; Moomaw, E. W.; Garcia-Rubio, I.; Ozarowski, A.; Krzystek, J.; Weber, R. T.; Richards, N. G. *J. Phys. Chem. B* **2007**, *111*, 5043. (c) Benmelouka, M.; van Tol, J.; Borel, A.; Port, M.; Helm, L.; Brunel, L. C.; Merbach, A. E. *J. Am. Chem. Soc.* **2006**, *128*, 7807.
(12) (a) Park, K.; Novotny, M. A.; Dalal, N. S.; Hill, S.; Rikvold, P. A. *Phys. Rev. B* **2002**, *65*, 014426. (b) Park, K.; Novotny, M. A.; Dalal, N. S.; Hill, S.; Rikvold, P. A. *Phys. Rev. B* **2002**, *66*, 144409.
(13) (a) Wang, Z.; Zheng, W.; van Tol, J.; Dalal, N. S.; Strouse, G. F. *Chem. Phys. Lett.* **2012**, *524*, 73−77. (b) Zheng, W.; Wang, Z.; Wright, J.; Goundie, B.; Dalal, N. S.; Meulenberg, R. W.; Strouse, G. F. *J. Phys. Chem. C* **2011**, *115*, 23305−23314.
(14) Ammam, M.; Keita, B.; Nadjo, L.; Mbomekalle, I.-M.; Fransaer, J. *J. Electroanal. Chem.* **2010**, *645*, 65−73.
(15) Keita, B.; Mbomekalle, I.-M.; Lu, Y. W.; Nadjo, L.; Berthet, P.; Anderson, T. M.; Hill, C. L. *Eur. J. Inorg. Chem.* **2004**, 3462−3475.
(16) (a) Perumareddi, J. R.; Liehr, A. D.; Adamson, A. W. *J. Am. Chem. Soc.* **1963**, *85*, 249−259. (b) Jeremy, K. B.; Hoffmann, R.; Fay, R. C. *Inorg. Chem.* **1978**, *17*, 2553−2568.
(17) Poblet, J. M.; López, X.; Bo, C. *Chem. Soc. Rev.* **2003**, *32*, 297−308. López, X.; Miró, P.; Carbó, J. J.; Rodríguez-Fortea, A.; Bo, C.; Poblet, J. M. *Theor. Chem. Acc.* **2011**, *128*, 393−404.
(18) Poblet, J. M.; Kortz, U. et al., to be published.
(19) Sheldrick, G. M. *Acta Crystallogr.* **2007**, *A64*, 112−122.
(20) Sheldrick, G. M. *SADABS, Program for empirical X-ray absorption correction*; Bruker-Nonius: Madison, WI, 1990.
(21) (a) Cage, B.; Hassan, A. K.; Pardi, L.; Krzystek., J.; Brunel, L. C.; Dalal, N. S. *J. Magn. Reson.* **1997**, *124*, 495−498. (b) van Tol, J.; Brunel, L. C.; Wylde, R. J. *Rev. Sci. Instrum.* **2005**, *76*, 074101.
(22) (a) Nellutla, S.; van Tol, J.; Dalal, N. S.; Bi, L.-H.; Kortz, U.; Keita, B.; Nadjo, L.; Khitrov, G. A.; Marshall, A. G. *Inorg. Chem.* **2005**, *44*, 9795−9806. (b) Mal, S. S.; Dickman, M. H.; Kortz, U.; Todea, A. M.; Merca, A.; Bögge, H.; Glaser, T.; Müller, A.; Nellutla, S.; Kaur, N.; van Tol, J.; Dalal, N. S.; Keita, B.; Nadjo, L. *Chem.—Eur. J.* **2008**, *14*, 1186−1195.
(23) Keita, B.; Nadjo, L. *J. Electroanal. Chem.* **1988**, *243*, 87−103.
(24) Frisch, M. J.; Trucks, G. W.; Schlegel, H. B.; Scuseria, G. E.; Robb, M. A.; Cheeseman, J. R.; Scalmani, G.; Barone, V.; Mennucci, B.; Petersson, G. A.; Nakatsuji, H.; Caricato, M.; Li, X.; Hratchian, H. P.; Izmaylov, A. F.; Bloino, J.; Zheng, G.; Sonnenberg, J. L.; Hada, M.; Ehara, M.; Toyota, K.; Fukuda, R.; Hasegawa, J.; Ishida, M.; Nakajima, T.; Honda, Y.; Kitao, O.; Nakai, H.; Vreven, T.; Montgomery, Jr., J. A.; Peralta, J. E.; Ogliaro, F.; Bearpark, M.; Heyd, J. J.; Brothers, E.; Kudin, K. N.; Staroverov, V. N.; Kobayashi, R.; Normand, J.; Raghavachari, K.; Rendell, A.; Burant, J. C.; Iyengar, S. S.; Tomasi, J.; Cossi, M.; Rega, N.; Millam, N. J.; Klene, M.; Knox, J. E.; Cross, J. B.; Bakken, V.; Adamo, C.; Jaramillo, J.; Gomperts, R.; Stratmann, R. E.; Yazyev, O.; Austin, A. J.; Cammi, R.; Pomelli, C.; Ochterski, J. W.; Martin, R. L.; Morokuma, K.; Zakrzewski, V. G.; Voth, G. A.; Salvador, P.; Dannenberg, J. J.; Dapprich, S.; Daniels, A. D.; Farkas, Ö.; Foresman, J. B.; Ortiz, J. V.; Cioslowski, J.; Fox, D. J. *Gaussian 09*, Revision A.1; Gaussian, Inc.: Wallingford, CT, 2009.
(25) (a) Lee, C.; Yang, C.; Parr, R. G. *Phys. Rev. B* **1988**, *37*, 785−789. (b) Becke, A. D. *J. Chem. Phys.* **1993**, *98*, 5648−5652. (c) Stephens, P. J.; Devlin, F. J.; Chabalowski, C. F.; Frisch, M. J. *J. Phys. Chem.* **1994**, *98*, 11623−11627.
(26) Hay, P. J.; Wadt, W. R. *J. Chem. Phys.* **1985**, *82*, 270−283.
(27) (a) Francl, M. M.; Pietro, W. J.; Hehre, W. J.; Binkley, J. S.; Gordon, M. S.; Defrees, D. J.; Pople, J. A. *J. Chem. Phys.* **1982**, *77*, 3654−3665. (b) Hehre, W. J.; Ditchfield, R.; Pople, J. A. *J. Chem. Phys.* **1972**, *56*, 2257−2261. (c) Hariharan, P. C.; Pople, J. A. *Theor. Chim. Acta* **1973**, *28*, 213−222.
(28) Marenich, A. V.; Cramer, C. J.; Truhlar, D. G. *J. Phys. Chem. B* **2009**, *113*, 6378−6396.

NOTE ADDED AFTER ASAP PUBLICATION

This paper was published on the Web on November 29, 2012, with minor text errors. The corrected version was reposted on November 30, 2012.